Please cite the following article as:

Hasan, S., Vasheghani Farahani, M., Van Offenwert, S., Bultreys, T., & Niasar, V. (2026). Comparative Evaluation of Models for Non-Fickian Transport in Unsaturated Porous Media. *InterPore Journal*. Advance online publication. https://doi.org/10.69631/fx3kjg18

Received on: 11 Nov. 2025
Accepted on: 29 Mar. 2026
Published online (Accepted version): 20 Apr. 2026

Comparative Evaluation of Models for Non-Fickian Transport in Unsaturated Porous Media

Sharul Hasan[†,a,b], Mehrdad Vasheghani Farahani[†,b], Stefanie Van Offenwert[c], Tom Bultreys[c], Vahid Niasar[*,b]

[*] *Corresponding author: vahid.niasar@manchester.ac.uk*

[†] *SH and MVF have equally contributed to this article.*

[a] *Department of Petroleum Engineering, Faculty of Chemical and Energy Engineering, Universiti Teknologi Malaysia, 81310 Johor Bahru, Johor, Malaysia*

[b] *Department of Chemical Engineering, University of Manchester, Oxford Road, Manchester, M13 9PL, UK*

[c] *Pore-scale Processes in Geomaterials Research Group (PProGRess), Department of Geology, Ghent University, Krijgslaan 281 S8, 9000 Ghent, Belgium*

Abstract

Understanding solute transport in unsaturated porous media is essential for a wide range of scientific and engineering applications. This study investigates non-Fickian transport in unsaturated porous media using pore-network modelling to simulate quasi-static two-phase flow and tracer transport. The pore-network model was first validated against experiments in glass bead packing. Then the validated model was used to simulate transport in three different hypothetical network structures with three different correlated pore-size distributions (characterised by correlation lengths), different Péclet (Pe) numbers, and saturation values. Breakthrough curve (BTC) analysis reveals an expected shift from anomalous long-tailed behaviour at low saturation to Fickian transport as saturation approaches unity.

The simulation results were interpreted using three continuum-scale approaches: Mobile Immobile (MIM), Multirate Mass Transfer (MRMT), Continuous Time Random Walk (CTRW), and their predictions were compared against each other and to direct estimations (DE) obtained from the pore-network simulations. Estimates of stagnant zone saturation from the MIM and MRMT models show strong sensitivity to saturation and flow conditions, at times yielding unrealistic values. Dispersion coefficients derived from the MIM and DE exhibit non-monotonic variation with saturation, consistent with both simulation trends and previously reported experimental observations, while the MRMT and CTRW models fail to capture this behaviour. The DE analysis demonstrates that mass transfer coefficients vary with time, challenging the assumption of constant rates in the MIM and

MRMT formulations. The findings underscore limitations of continuum-scale models and emphasise the role of two-phase flow distributions, time-dependent mass transfer, and saturation-dependent dispersion in accurately predicting transport in unsaturated media.

1. Introduction

Fluid flow and mass transfer in porous media are ubiquitous phenomena in a variety of natural and engineering systems, such as hydrology, agriculture, chemical engineering, biology, and the energy industry (Sahimi, 1993; Lima et al., 2008; Babaei and Joekar-Niasar, 2016). Accurate quantification and prediction of the performance of such processes require a profound understanding of how a tortuous assembly of interconnected pores would affect the transport of a solute by a carrying fluid through them (Souzy et al., 2020; Yoon and Kang, 2021). Solute transport by a carrying fluid occurs through advection, governed by fluid velocity, and diffusion, driven by concentration gradients and Brownian motion of solute molecules. Each mechanism has its own characteristic time scale, and their relative importance is characterised by the Péclet number (Pe), which is the ratio of advective to diffusive transport.

Solute transport in saturated (single phase) porous media is complex, primarily due to the interaction of the carrying fluid with the spatially variable pore size and hydraulic conductivity, resulting in a non-uniform velocity field and solute dispersion, a behaviour typically described by a single advection-dispersion equation (Amin et al., 1997; Capuani et al., 2003; Fallico, 2012; Erfani et al., 2019; Zhang et al., 2019). Further complexities arise in unsaturated (multiphase) and/or heterogeneous porous media, in which, depending on the flow conditions, the connectivity of the pore space, and the distribution of the carrying phase, preferential flow pathways (mobile zones) provide a substantial contribution to the fluid flow and transport through the advection mechanism, whereas stagnant regions (immobile zones) may poorly contribute through the diffusion mechanism. These complexities lead to multiple characteristic transport timescales, hence anomalous or non-Fickian behaviours, such as long tails in the solute breakthrough curve (BTC), nonlinear evolution of dispersion and its dependence on the phase saturation topology (Biggar and Nielsen, 1960; Bijeljic et al., 2013; Aziz et al., 2018; Ben-Noah et al., 2023).

The advection-dispersion equation (ADE) is unable to describe non-Fickian transport in unsaturated porous media at the continuum scale because it does not incorporate two-

phase flow properties, which significantly impact transport characteristics (Karadimitriou et al., 2016). Thus, alternative approaches, such as the mobile-immobile model (MIM), the multirate mass transfer model (MRMT), and the continuous-time random walk model (CTRW), have been adapted, as inverse modelling tools, to characterise non-Fickian dispersive transport in porous media under two-phase conditions (Gao et al., 2009b; Dentz et al., 2004). In the MIM and MRMT models, considering non-equilibrium mass transfer between mobile and immobile zones enables capturing early solute breakthrough through mobile zones and long tails in solute BTCs caused by diffusive mass transfer from immobile zones to mobile regions (Coats and Smith, 1964; Baker, 1977; van Genuchten and Wierenga, 1976; Haggerty and Gorelick, 1995). The average pore velocity, longitudinal dispersion coefficient, stagnant saturation, and mass transfer rate(s) are determined by fitting the BTC to the transport models (Raoof and Hassanizadeh, 2013; Muniruzzaman and Rolle, 2017; Wang et al., 2019; Chen et al., 2019; Zhuang et al., 2021). The MRMT model can be viewed as a generalised form of the MIM approach, introducing multiple immobile zones, each characterised by different mass transfer rates. This allows MRMT to account for different rate coefficients rather than a single value, making it particularly suitable for highly heterogeneous systems, such as fractured porous structures, where solutes experience a wide range of residence behaviours (Tecklenburg et al., 2016). The CTRW model has been developed based on the fact that the residence time of a solute particle in low-velocity regions is longer than in high-velocity zones and that the velocity changes in space only (not in time) on a characteristic length scale (Saffman, 1959; Scher and Lax, 1973; Berkowitz et al., 2008). In this model, the solute transport is described through spatiotemporal particle transitions, steps where a particle moves a certain distance and pauses for a random residence time, whose time distribution reflects mass transfer behaviour (Ben-Noah et al., 2023). The CTRW model does not relate solute transport in diffusive-dominated zones to stagnant saturation and mass transfer rate(s); instead, it uses a power-law equation to capture the behaviour over time. This is why stagnant saturation and mass transfer rates estimated from the CTRW model cannot be directly compared against those estimated by the MIM and MRMT models (Bromly and Hinz, 2004; Gao et al., 2009b). The CTRW model has been successfully used as an inverse model to characterise non-Fickian transport due to heterogeneity (Cortis and Birkholzer, 2008; Berkowitz and Scher, 2009; Berkowitz et al., 2009; Gao et al., 2009b)

and solute transport under unsaturated conditions (Bromly and Hinz, 2004; Zoia et al., 2010; Ben-Noah et al., 2023). While the above models have been extensively used to describe non-Fickian transport, their physical consistency still needs to be comprehensively evaluated (Hasan et al., 2020).

Recent experimental and numerical studies have demonstrated that stagnant zone saturation and mass transfer between mobile and immobile zones can be directly estimated by characterising solute transport in low- and high-velocity regions within unsaturated porous media (Karadimitriou et al., 2016, 2017; Aziz et al., 2018; Hasan et al., 2019; Van Offenwert et al., 2024). This approach, referred to as the Direct Estimation (DE), uses a passive tracer as the solute, and its transport is characterised under steady-state saturation conditions, meaning that phase saturation values remain constant. Comparisons between DE-derived transport parameters and those obtained from the MIM model revealed that the stagnant saturation estimated by the MIM model varies with changes in the hydrodynamic conditions (characterised by Pe), even when the saturation topology remains unchanged (Hasan et al., 2019). Furthermore, it was shown that the MIM model cannot explicitly incorporate two-phase flow properties in describing solute transport, as it is a phenomenological model that infers stagnant saturation solely from the BTC shape. In this work, we extend the above findings by systematically comparing the performance of the MIM, MRMT, and CTRW in predicting solute transport properties under two-phase flow conditions, and by evaluating their predictions against those obtained from the DE. We use pore-network modelling (PNM), owing to its ability to simulate transport in large domains with manageable computational cost, as an upscaling tool to simulate solute transport in three-dimensional (3D) unsaturated porous media, thereby obtaining BTCs and directly determining stagnant saturation, mass transfer rates, and solute concentrations in flowing and stagnant regions under different hydrodynamic conditions. This work provides new insight into the accuracy, validity, and applicability of the above commonly used non-Fickian models for describing solute transport in unsaturated porous media.

2. The physical framework of continuum-scale two-phase transport models

In this section, we provide a brief review of the physical framework of the MIM, MRMT, and CTRW models, which are extensively used to characterise solute transport in unsaturated porous media. Additionally, we review the physical framework of the DE,

focusing on the procedures for obtaining stagnant saturation and mass transfer rates.

2.1. Mobile-immobile model (MIM)

The MIM model was first developed by van Genuchten and Wierenga (1976) to characterise chemical transport through an unsaturated porous medium. In this model, the pore space is divided into two distinct regions based on pore velocity: (i) flowing (mobile) zones and (ii) stagnant (immobile) zones (An et al., 2020a; Saeibehrouzi et al., 2024). The full set of equations for non-reactive solute transport in the MIM model can be written as:

$$\frac{\partial C_\mathrm{f}}{\partial t} + \left(\frac{S_\mathrm{s}}{S - S_\mathrm{s}}\right)\frac{\partial C_\mathrm{s}}{\partial t} = D\frac{\partial^2 C_\mathrm{f}}{\partial x^2} - v\frac{\partial C_\mathrm{f}}{\partial x} \tag{1}$$

$$S_\mathrm{s}\phi\frac{\partial C_\mathrm{s}}{\partial t} = \gamma(C_\mathrm{f} - C_\mathrm{s}) \tag{2}$$

where C is concentration, S is saturation of the solute-carrying fluid phase, and the subscripts f and s denote its flowing and stagnant portions, respectively ($S = S_\mathrm{f} + S_\mathrm{s}$). D is the longitudinal dispersion coefficient, v is the average mobile pore velocity, γ is the first-order mass transfer coefficient, and ϕ is porosity. It can be seen that Equation (1) extends the classical ADE by incorporating the non-equilibrium mass transfer between the flowing and stagnant zones, herein referred to as the source-sink term, and Equation (2) accounts for this new term. Several experimental and modelling studies have employed the MIM model to describe non-Fickian transport in unsaturated porous media (Maraqa et al., 1997; Padilla et al., 1999; Toride et al., 2003; Gao et al., 2009a; Babaei and Islam, 2018; Su, 2012; Dou et al., 2021). In this work, transport parameters (S_s, D, v, and γ) were estimated by inverse modelling using a modified version of the CXTFIT code implemented in the STANMOD package (Toride et al., 1995; Van Genuchten et al., 2012). In this framework, Equations (1) and (2) are reduced to analytical solutions under the prescribed initial and boundary conditions by reformulating the governing equations in dimensionless form, following the approach of Toride et al. (1995). These analytical solutions serve as the forward model in the inverse problem. Parameter estimation is then carried out by minimising the squared difference between the simulated BTCs and the model predictions using a non-linear least-squares optimisation algorithm.

2.2. Multirate mass transfer model (MRMT)

The long tailing of BTC in non-Fickian transport through a non-adsorbing porous system can result from the presence of several stagnant zones, each with unique characteristics and mass transfer rate (Haggerty and Gorelick, 1995, 1998). To account for this, Equations (1) and (2) can be extended to include N stagnant zones, each characterised by a unique mass transfer coefficient γ_j:

$$\frac{\partial C_\mathrm{f}}{\partial t} + \sum_{j=1}^{N} \sigma_j \frac{\partial (C_\mathrm{s})_j}{\partial t} = D\frac{\partial^2 C_\mathrm{f}}{\partial x^2} - v\frac{\partial C_\mathrm{f}}{\partial x} \tag{3}$$

$$(S_\mathrm{s})_j \phi \frac{\partial (C_\mathrm{s})_j}{\partial t} = \gamma_j \left(C_\mathrm{f} - (C_\mathrm{s})_j\right) \tag{4}$$

in which σ_j is the capacity coefficient of the stagnant zone j, defined as the ratio of its saturation to the flowing saturation (Haggerty and Gorelick, 1995):

$$\sigma_j = \frac{(S_\mathrm{s})_j}{S - (S_\mathrm{s})_j}. \tag{5}$$

While the source-sink term is typically expressed as the derivative of stagnant concentration with respect to time, as shown in Equations (3) and (4), an alternative formulation proposed by Haggerty et al. (2000) uses a convolution integral to express the source-sink in terms of a memory function, $g(t)$:

$$g(t) = \int_0^\infty \gamma b(\gamma) e^{-\gamma t} d\gamma \tag{6}$$

and the derivative of flowing concentration with respect to time. In Equation (6), $b(\gamma)$ is a density function of the mass transfer coefficient γ, which can be described by a power-law equation:

$$b(\gamma) = \frac{\sum_{j=1}^{N} \sigma_j (k-2)}{\gamma_{max}^{k-2} - \gamma_{min}^{k-2}} \gamma^{k-3} \quad k > 0, k \neq 2, \gamma_{min} \leq \gamma \leq \gamma_{max} \tag{7}$$

where k is an exponent, and γ_{min} and γ_{max} are the minimum and maximum mass transfer coefficients, respectively (Haggerty et al., 2000).

In the MRMT framework, the governing transport equations are reformulated using a memory function that represents the superposition of mass transfer processes associated with a continuous distribution of stagnant regions. Under the prescribed initial and boundary conditions, this formulation yields a semi-analytical solution in which the

source–sink term is expressed through a convolution integral involving the memory function (Equation (6)). These semi-analytical expressions serve as the forward model for inverse analysis. Transport parameters, including the dispersion coefficient D and the parameters defining the mass transfer rate distribution (e.g. $\gamma_{\min}$, $\gamma_{\max}$, and k), are estimated by fitting the model predictions to the breakthrough curves using a non-linear least-squares optimisation algorithm. In this study, the inverse modelling was performed using the STAMMT-L code (Haggerty, 2009), which efficiently evaluates the semi-analytical MRMT solution without requiring explicit numerical discretisation of the governing equations.

2.3. Continuous time random walk model (CTRW)

In the CTRW model, the ADE for solute transport is represented by a Generalised Master Equation in the Laplace transformed space of the time variable t, with the Laplace variable denoted by u and Laplace transformed quantities by $\sim$ (Dentz and Berkowitz, 2003; Cortis and Berkowitz, 2004):

$$u\tilde{c}(x,u) - c_0(x) = -\tilde{M}(u)\left[v_\psi \frac{\partial \tilde{c}(x,u)}{\partial x} - D_\psi \frac{\partial^2 \tilde{c}(x,u)}{\partial x^2}\right] \tag{8}$$

In the above equation, D_ψ and v_ψ are the Laplace transformed dispersion coefficient and the pore velocity, respectively, $c_0(x)$ is the initial concentration and $\tilde{c}$ is the Laplace transformed concentration. $\tilde{M}(u)$ is a memory function accounting for the unknown heterogeneities at the pore scale, defined as:

$$\tilde{M}(u) = \bar{t}u\frac{\tilde{\psi}(u)}{1-\tilde{\psi}(u)} \tag{9}$$

where $\bar{t}$ is the characteristic time. $\tilde{\psi}(u)$ in Equation (9) is the Laplace transform of a truncated power-law (TPL) probability distribution function $\psi(t)$, describing each solute particle transition with time:

$$\tilde{\psi}(u) = (1+\tau_2 u t_1)^\beta \exp(t_1 u)\Gamma(-\beta, \tau_2^{-1} + t_1 u)/\Gamma(-\beta, \tau_2^{-1}) \tag{10}$$

In the above equation, $\tau_2 \equiv t_2/t_1$, β is the exponent determining the nature of the dispersion (Fickian at $\beta > 2$ and non-Fickian at $0 < \beta < 2$) (Dentz et al., 2004; Cortis and Berkowitz, 2004), and Γ is the incomplete Gamma function (Cortis and Berkowitz, 2004). The parameter t_1 is the average time for a solute particle to move from one pore to

another (Dentz et al., 2004), and t_2 is the cut-off time, separating transport in advective-dominated (flowing) zone from that in diffusive-dominated (stagnant) zone (Dentz et al., 2004).

The CTRW governing equation is formulated in the Laplace domain and is transformed numerically into the time domain under the prescribed initial and boundary conditions. In this study, the time-domain solution was evaluated using the CTRW MATLAB Toolbox v4.0 (Cortis et al., 2017), which employs numerical Laplace inversion techniques to compute breakthrough curves. Model parameters β, t_1, t_2, v_ψ, and D_ψ were estimated via inverse modelling by fitting the simulated breakthrough curves to the numerical CTRW solution. Parameter optimisation was performed using the toolbox's built-in error minimisation algorithm, which iteratively adjusts the CTRW parameters to minimise the misfit between the predicted and observed BTCs.

2.4. Direct estimation (DE)

The direct estimation (DE) approach was first introduced by Karadimitriou et al. (2016) and used to characterise non-Fickian solute transport in two-dimensional (2D) unsaturated porous media, and expanded to 3D porous media by Hasan et al. (2019) and An et al. (2020a). To directly estimate the stagnant saturation in the DE, steady-state two-phase saturation conditions must first be established, ensuring that the saturation values of the phases remain constant over time. Under these conditions, a tracer is injected into one of the fluid phases, typically the aqueous/non-wetting phase. As the tracer moves through the porous medium, two distinct zones appear: the flowing zone, dominated by advective transport, and the stagnant zone, where transport is predominantly diffusion-controlled. This means that, unlike the above models that rely solely on breakthrough curve (BTC) fitting, DE requires detailed spatial information about flow and/or transport within the domain. Although this makes the approach more data intensive, it also allows the underlying pore-scale physics to be explicitly incorporated, leading to more physically consistent and reliable estimates of transport parameters (Karadimitriou et al., 2016; An et al., 2020b).

To evaluate transport characteristics, local pore velocities obtained from PNM are extracted and their histogram is plotted at different S values, which typically shows a bimodal distribution at intermediate saturations ($0 \ll S \ll 1$) with the first peak representing the stagnant zone and the second peak representing the flowing zone, and

a unimodal distribution when $S \rightarrow 0$ or 1 (Aziz et al., 2018; Hasan et al., 2019; An et al., 2020a; Velásquez-Parra et al., 2022). The grouped plot of the local pore velocity histograms is then analysed to find a threshold velocity that separates the first and second peaks. Using this threshold as a guide, a search algorithm is applied to obtain the stagnant saturation, which is defined as:

$$S_{\mathrm{s}} = \frac{\sum_{u<\bar{v}} r_{ij}^2 l_{ij}}{\sum r_{ij}^2 l_{ij}} + \frac{\sum_{u<\bar{v}} R_i^3}{\sum R_i^3}. \tag{11}$$

In this equation, $\bar{v}$ is the threshold velocity, l_{ij} is the length of the pore throat connecting pore bodies i and j, r_{ij} and R_i are the radii of pore throats ij and pore bodies i, respectively, and u represents the local pore velocity. Hasan et al. (2019) proposed that relative permeability-saturation curves bear important information about the stagnant saturation and established a scaling between their stagnant saturation and total relative permeability. The stagnant saturation can be also directly estimated by using real-time visualisation of solute transport, through identifying zones delayed in mixing (stagnant zones) and those that have reached the injection solute concentration (flowing zones) (Karadimitriou et al., 2016; Jiménez-Martinez et al., 2017; Van Offenwert et al., 2024).

In this work, we utilised the first approach, in which the histogram of local pore velocities is obtained at different saturations to find $\bar{v}$, followed by using Equation (11) to calculate S_{s}, and Equations (12):

$$C_{\mathrm{f}} = \frac{\sum_{u\geq\bar{v}} C_i V_i}{\sum V_i} \tag{12}$$

and (13):

$$C_{\mathrm{s}} = \frac{\sum_{u<\bar{v}} C_i V_i}{\sum V_i} \tag{13}$$

to obtain C_{f} and C_{s}, respectively. In Equations (12) and (13), C_i and V_i are the solute concentration in and the volume of pore body i and half of its neighbouring pore throats. Eventually, Equation (2) is rearranged to determine γ:

$$\gamma(t) = \frac{S_{\mathrm{s}}\phi}{C_{\mathrm{f}} - C_{\mathrm{s}}} \frac{\partial C_{\mathrm{s}}}{\partial t}. \tag{14}$$

When using DE, we first characterise the stagnant and flowing zones for a given saturation. A threshold time, defined as the time when the solute in the flowing zone

reaches 0.99, is then identified to separate the solute transport in these two zones. Using this time, the portion of the effluent flux-averaged BTCs affected by solute transport in the flowing zone, attributed to the Fickian transport (An et al., 2020b), is fitted to the analytical solution of the advection-dispersion equation (Ogata and Banks, 1961):

$$\langle C^f_{OB}(x,t)\rangle = \frac{1}{2}C_{\max}\left[\operatorname{erfc}\left(\frac{x-vt}{2\sqrt{Dt}}\right) + \exp\left(\frac{vx}{D}\right)\operatorname{erfc}\left(\frac{x+vt}{2\sqrt{Dt}}\right)\right] \tag{15}$$

to obtain D and v.

At a given saturation S, the presence of stagnant zones can cause breakthrough curves to exhibit strong skewness at early and/or late times, which may adversely affect the inverse optimisation used to fit the transport models. The quantity $\langle C^f(t)\rangle$ is normalised by the inlet concentration and therefore varies between 0 and 1. Values of $\langle C^f(t)\rangle$ smaller than 10^{-5} and larger than 0.99 were excluded from the fitting procedure solely to improve numerical robustness and parameter identifiability, as these extreme early- and late-time data points are particularly sensitive to tailing effects and numerical noise.

The DE is inherently more computationally demanding than continuum-scale inverse models, as it requires detailed pore-scale information on velocity fields, saturation distributions, and/or transient solute concentrations. In this work, these quantities are obtained from pore-network simulations, although equivalent information may also be acquired experimentally using high-resolution imaging and tracer visualisation techniques (Karadimitriou et al., 2016; Jiménez-Martinez et al., 2017; Van Offenwert et al., 2024). From a computational perspective, the dominant cost arises from resolving steady-state two-phase flow and transient solute transport at the pore scale, followed by post-processing steps such as velocity histogram analysis, phase partitioning, and time-dependent mass transfer estimation. These requirements currently limit the direct application of DE to small domains, typically at the millimetre scale, where pore-scale resolution is feasible. Nevertheless, DE is not intended as a replacement for continuum-scale transport models in field applications. Rather, it provides a physically grounded benchmark that enables direct quantification of stagnant saturation, dispersion, and mass transfer dynamics based on pore-scale transport mechanisms. Recent advances in pore-scale modelling and high-performance computing have demonstrated that pore-resolved simulations can be extended to centimetre-scale domains, such as core-scale systems, thereby expanding the range of conditions under which DE-derived insights can be obtained (Mahmoodlu et al.,

2020).

3. Methodology

3.1. Pore-network models

In this study, we adopted the procedure detailed by Babaei and Joekar-Niasar (2016) to generate pore networks. Briefly, the topology of the networks was first created using 3D Delaunay triangulation, where the vertices represent the positions of pore bodies and the edges represent the pore throats. Next, excessively long pore throats were identified and removed such that a realistic mean coordination number is generated. Finally, a correlation length (λ) field generator was used to specify the sizes of the pore bodies and throats. Following the above procedure, three pore networks with dimensions of $15 \times 15 \times 15$ mm^3 and over a million pore bodies were generated: a homogeneous uncorrelated network ($\lambda = 0.0$ mm) and two heterogeneous correlated ($\lambda = 0.375$ mm and 0.75 mm) networks. The corresponding absolute permeabilities were 10.50 mD, 15.23 mD, and 16.87 mD, respectively (An et al., 2020b). The generated networks and their relative frequency of the pore body and throat sizes are shown in Figure 1 and their statistical details are tabulated in Table 1. It is emphasised that the pore networks have the same topology but different spatial distribution of pore bodies and throats.

Table 1: Statistical details of the pore body and thorat sizes of the generated pore networks.

λ (mm)	Pore body statistics		Pore throat statistics	
	Mean (mm)	Standard deviation (mm)	Mean (mm)	Standard deviation (mm)
0	0.0156	8.61×10^{-3}	0.0056	2.45×10^{-3}
0.375	0.0156	8.58×10^{-3}	0.0061	3.24×10^{-3}
0.75	0.0156	8.53×10^{-3}	0.0063	3.45×10^{-3}

3.2. Steady state two-phase flow and solute transport simulation

We followed the methodology detailed by An et al. (2020a) to simulate solute transport in a pore network under two-phase flow conditions. The process starts by establishing steady-state saturation conditions, achieved by displacing the receding fluid (wetting phase) with the invading fluid (non-wetting phase). The displacement is governed by

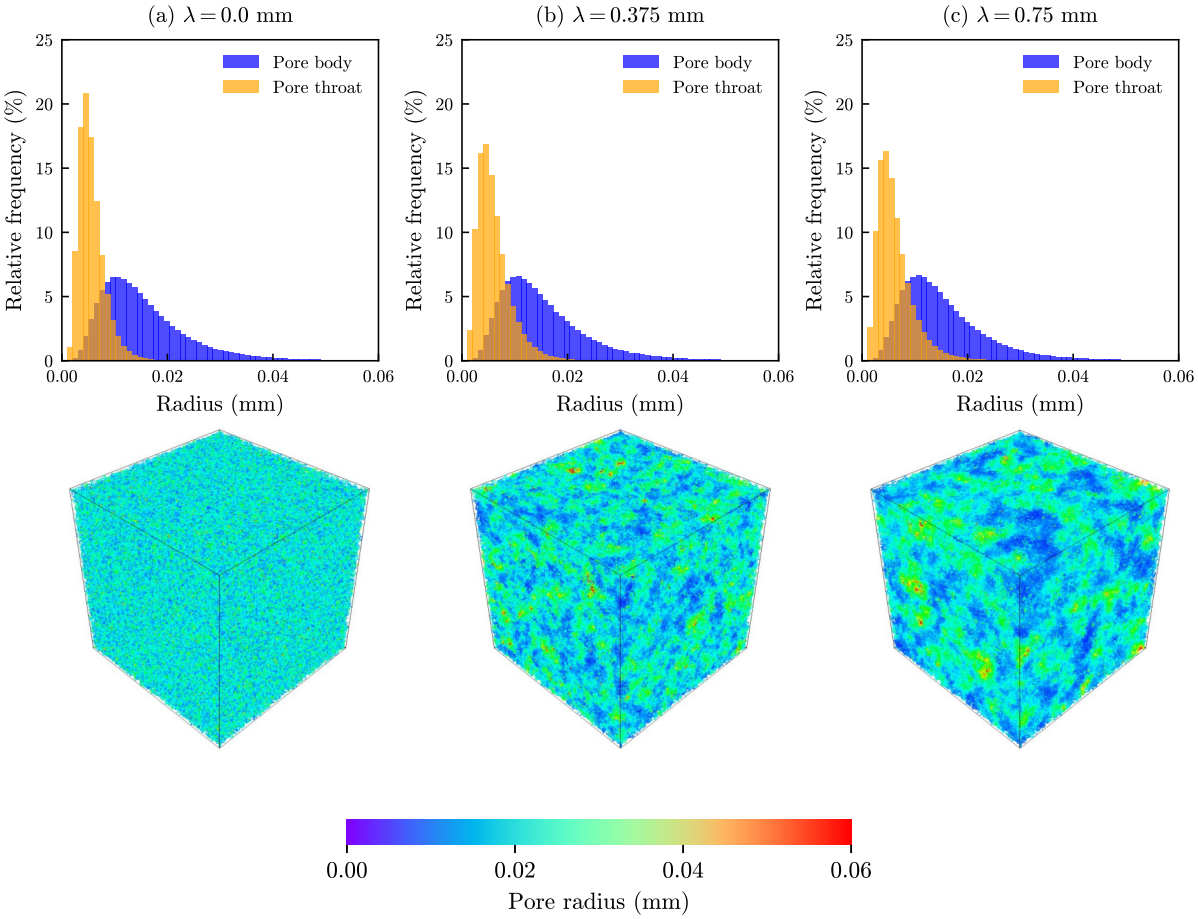

Figure 1: Relative frequency of pore body and throat sizes of the generated pore networks and their respective pore-network topology. The uncorrelated domain ($\lambda = 0.0$ mm) has an absolute permeability of 10.50 mD, while the correlated domains with $\lambda = 0.375$ mm and $\lambda = 0.75$ mm have permeabilities of 15.23 mD and 16.87 mD, respectively.

the entry capillary pressure, calculated for pore throats using the Young–Laplace equation. Different saturation states are obtained by progressively invading the pore network according to the entry capillary pressure criterion until a target steady-state saturation is reached. Upon establishing the steady-state saturation field throughout the domain, solute, dissolved in the invading fluid, is injected from the inlet. We highlight that the solute is assumed to be soluble only in the invading fluid; therefore, no inter-phase mass transfer is considered during solute transport. Such a configuration is representative of situations in which solutes are transported within non-wetting carrier fluids, including surfactant or tracer transport in aqueous phases during enhanced oil recovery in oil-wet reservoirs (Al-Azani et al., 2022), and organic contaminant transport within non-aqueous phase liquids (NAPLs) in subsurface remediation (Leharne, 2019; Mineo, 2023).

To simulate solute transport, the classical ADE with the Taylor–Aris dispersion cor-

rection factor (Bello et al., 1994; Hekmatzadeh et al., 2016; Hasan et al., 2019) is solved only for pores occupied by the invading fluid, with Dirichlet boundary conditions being applied at the inlet ($C|_{\text{in}}= 1.0$) and zero-gradient boundary conditions imposed at the outlet ($C_i - C|_{\text{out}}= 0.0$), to compute temporally evolving local pore concentrations. For pore body i, the conservation equation for the concentration can be expressed as follows:

$$V_i \frac{\partial C_i}{\partial t} = \sum_{q_{ij}<0} q_{ij} C_i + \sum_{q_{ij}>0} q_{ij} C_j + \sum_{j \in N_i} \pi r_{ij}^2 D_{ij} \left(\frac{C_j - C_i}{l_{ij}} \right) , \quad \{i, j\} \in \Omega_{\text{invading fluid}} \tag{16a}$$

$$D_{ij} = D_m (1 + \kappa Pe_{ij}^2) , \quad \kappa = 1/192 \tag{16b}$$

where C_i is the solute concentration in pore body i, D_{ij} is the Taylor–Aris dispersion coefficient, D_m represents molecular diffusion, and N_i denotes the coordination number of pore body i (the number of pore throats connected to pore body i). The summation over $j \in N_i$ therefore accounts for diffusive mass exchange between pore body i and all its directly connected neighbouring pore bodies through the associated pore throats. The local Pe number is defined as $Pe_{ij} = v_{ij} r_{ij}/D_m$ with v_{ij} being the average pore velocity in the pore throat ij. The volumetric flow rate q_{ij} between pore bodies i and j is obtained by solving the steady-state flow problem on the pore network, restricted to regions occupied by the invading phase, prior to the transport simulation. Flow through each pore throat is assumed to be laminar, and q_{ij} is calculated using a Hagen–Poiseuille-based conductance formulation as a function of the pressure difference between connected pore bodies (Valvatne and Blunt, 2004):

$$q_{ij} = \frac{A_{ij}^2 G_{ij}}{2\mu l_{ij}} (P_i - P_j), \tag{17}$$

where A_{ij} is the cross-sectional area of the pore throat, μ is the viscosity of the carrying fluid, and P_i and P_j are the pressures in pore bodies i and j, respectively. The shape factor G_{ij} accounts for the throat geometry and is determined directly from the extracted pore-network geometry as $G_{ij} = V_{ij} l_{ij}/A_s^2$, where V_{ij} is the pore throat volume and A_s is its surface area. These geometric quantities are obtained from image-processing-based pore-network extraction methods following the procedure described by Dong and Blunt (2009).

It should be noted that the following simplifying assumptions apply when solving the ADE: (i) the flow through pore throats is considered laminar, hence the Hagen-Poiseuille equation can be used to compute the pore velocities, (ii) pore bodies are spherical and pore throats are cylindrical, (iii) pore bodies have no resistance against the flow compared to the pore throats, and (iv) complete mixing occurs in pore bodies. Under these assumptions, Equation (16b) follows from the classical Taylor–Aris dispersion theory, which predicts that dispersion in a cylindrical tube scales with the square of the mean fluid velocity, and hence with Pe^2. A further requirement of the Taylor–Aris formulation is that transverse diffusive mixing across the pore throat cross-section occurs sufficiently rapidly compared to axial advection. For the pore throat sizes and molecular diffusion coefficient considered here, the characteristic transverse diffusion timescale, $t_d \sim r_{ij}^2/D_m$, is much smaller than the advective residence time within individual pore throats. The use of the Taylor–Aris dispersion correction is therefore appropriate over the temporal and spatial scales investigated in this study. We note that in real porous media, dispersion commonly exhibits a weaker, sub-quadratic dependence on Pe due to pore-scale heterogeneity, tortuous flow paths, and enhanced mixing in complex geometries. Such effects are not explicitly represented in idealised Poiseuille tube models and may lead to deviations from the Pe^2 scaling observed in experimental systems (Li et al., 2006; Liu et al., 2024; Singh and Obi, 2025).

The average resident concentration $\langle C^r(t)\rangle$ at time t is then calculated by averaging the pore concentrations, weighted by the pore volume V_i:

$$\langle C^r(t)\rangle = \frac{\sum C_i(t)V_i}{\sum V_i}, i \in \Omega_{\text{invading fluid}}. \tag{18}$$

The effluent flux-averaged concentration $\langle C^f(t)\rangle$ is also calculated by averaging the concentrations at outlet pores C_{ij}, weighted by q_{ij}:

$$\langle C^f(t)\rangle = \frac{\sum C_{ij}(t)q_{ij}}{\sum q_{ij}}, ij \in \Omega_{\text{outflow boundary}}. \tag{19}$$

The parameters $\langle C^r(t)\rangle$ and $\langle C^f(t)\rangle$ can be then plotted versus time to obtain resident and flux-averaged BTCs. The effluent flux-averaged concentration BTC is finally fitted to the solute transport models (see Section 2) in order to obtain the fitting parameters and characterise the nature of the transport. It should be noted that a criterion of $R^2 > 0.98$ was applied in this work for the BTC fitting and inverse modelling to ensure the reliability

of the fitted parameters (R^2 values available in the Supporting Information).

The simulations were conducted at a wide range of the invading (solute-carrying) non-wetting phase saturation values and differential pressures of 10, 50, and 100 kPa for all three pore networks, corresponding to the pressure gradients of 0.667, 3.333, and 6.667 MPa/m, respectively. Only saturation values $S > 0.3$ were considered, which were chosen to be well above the percolation threshold of the invading phase, thereby ensuring the presence of a continuous spanning cluster that enables solute transport across the domain. It should be noted that varying saturation through the immiscible displacement process modifies pore-scale connectivity and flow pathways, leading to systematic variations in characteristic velocities and transport regimes under a given differential pressure. Under pressure-driven conditions, this behaviour is consistent with Darcy's law for multiphase flow, $\mathbf{v}^\alpha = -(k\, k_r^\alpha/\mu^\alpha)\nabla P$, where k is the absolute permeability, k_r^α is the relative permeability of phase α, and μ^α is its viscosity (An et al., 2020a). For a fixed imposed pressure gradient, the characteristic velocity of the solute-carrying phase therefore scales with its relative permeability, i.e. $\mathbf{v}^\alpha \propto k_r^\alpha$. Such conditions are representative of subsurface transport problems in partially saturated porous media, where a prescribed pressure gradient is applied and solute migration occurs within the connected phase while saturation-dependent pore connectivity evolves.

For each imposed ΔP, the corresponding Pe numbers were calculated at different S values using the Equation (20):

$$Pe = \frac{v_{in} l_c}{D}, \tag{20}$$

where v_{in} is the average inlet velocity, $l_c = 15$ mm is the characteristic length, and $D = 10^{-9}\,\mathrm{m^2 s^{-1}}$ is the diffusion coefficient. The characteristic length l_c corresponds to the length of the pore network and is used here to define a macroscopic (continuum-scale) Pe number based on the advective residence time across the domain. This definition is consistent with the MIM, MRMT, and CTRW models discussed in Section 2, which work at the continuum scale and do not explicitly resolve pore-scale length scales. While saturation alters pore-scale connectivity and local transport pathways, its effect on the macroscopic Pe number is captured through the saturation-dependent inlet velocity v_{in} rather than through a variable characteristic length. A similar definition of l_c was adopted by Huysmans and Dassargues (2005). Table 2 summarises the calculated Pe numbers for

each pore network under varying saturation and differential pressure conditions.

Table 2: Pe numbers for the three pore networks at different saturation (S) and differential pressure (ΔP) conditions.

Pe values for uncorrelated network ($\lambda = 0.0$ mm)					
ΔP (kPa)	$S = 0.41$	$S = 0.49$	$S = 0.62$	$S = 0.75$	$S = 0.94$
10	1.95	4.20	14.25	37.65	92.40
50	9.75	21.45	71.85	187.80	461.85
100	19.50	42.75	143.70	375.60	923.70

Pe values for correlated network ($\lambda = 0.375$ mm)					
ΔP (kPa)	$S = 0.35$	$S = 0.48$	$S = 0.61$	$S = 0.80$	$S = 0.95$
10	2.10	7.35	20.55	71.85	136.80
50	10.95	36.75	102.75	359.70	684.15
100	21.90	73.65	205.50	719.40	1368.45

Pe values for correlated network ($\lambda = 0.75$ mm)				
ΔP (kPa)	$S = 0.31$	$S = 0.59$	$S = 0.80$	$S = 0.96$
10	4.20	27.60	83.10	147.30
50	21.30	138.45	415.35	736.95
100	42.75	276.90	830.85	1474.35

3.3. Validation of the pore-network model

We validated the above methodology by comparing its performance in predicting solute transport behaviour in a porous medium against the experimental results reported by Van Offenwert et al. (2019). The experimental study used fast X-ray micro-CT imaging to quantify transient solute concentration fields in a saturated porous medium (sintered glass with pore sizes of 150 - 250 μm, ROBU P0, Germany). An X-ray micro-CT image of the dry sample, with dimensions of 6.0 mm in diameter and 5.0 mm in length and a porosity of 0.23, was used to extract a pore-network model using distance map, maximal ball, and watershed algorithms (Raeini et al., 2017). The extracted network had cylindrical

pore throats and spherical pore bodies, with a porosity of 0.22, similar to that of the real porous medium.

Solute transport was simulated in the pore network at two injection rates of 0.25 and 0.50 μl s^{-1}, identical to the experimental conditions (Van Offenwert et al., 2019). To account for the delay in solute concentration reaching unity at the inlet, which was observed experimentally (possibly due to the solute dispersion within the injection line), Equation (21) was used to specify the concentration values at the inlet pores:

$$C(t)|_{\text{in}} = \frac{\exp(a(t-b))}{\exp(a(t-b))+1}, \tag{21}$$

in which a and b are the fitting coefficients, determined by fitting the equation to the experimental data (see Supporting Information for more details). The steady-state volumetric flow rates q_{ij}, computed using Equation (17), were then used to formulate the mass balance for each pore body and to resolve advective solute transport and the temporal evolution of C_i. Eventually, relative $\langle C^r(t)\rangle$ (Equation (18)) was obtained and plotted over time and injected pore volume of the invading fluid, PVI, obtained by scaling t by the advective characteristic time:

$$t_{ad} = \frac{V_p S}{Q}, \tag{22}$$

together with the experimentally determined results in Figure 2. As can be seen, the simulation results have an excellent agreement with the experimental data at both solute injection rates, confirming the accuracy of the approach. We highlight that although the validation is performed under fully saturated conditions, it remains relevant because solute transport simulations in the unsaturated cases are conducted only after the immiscible displacement process has reached steady state (see Section 3.2), with the solute assumed to be soluble exclusively in the invading phase.

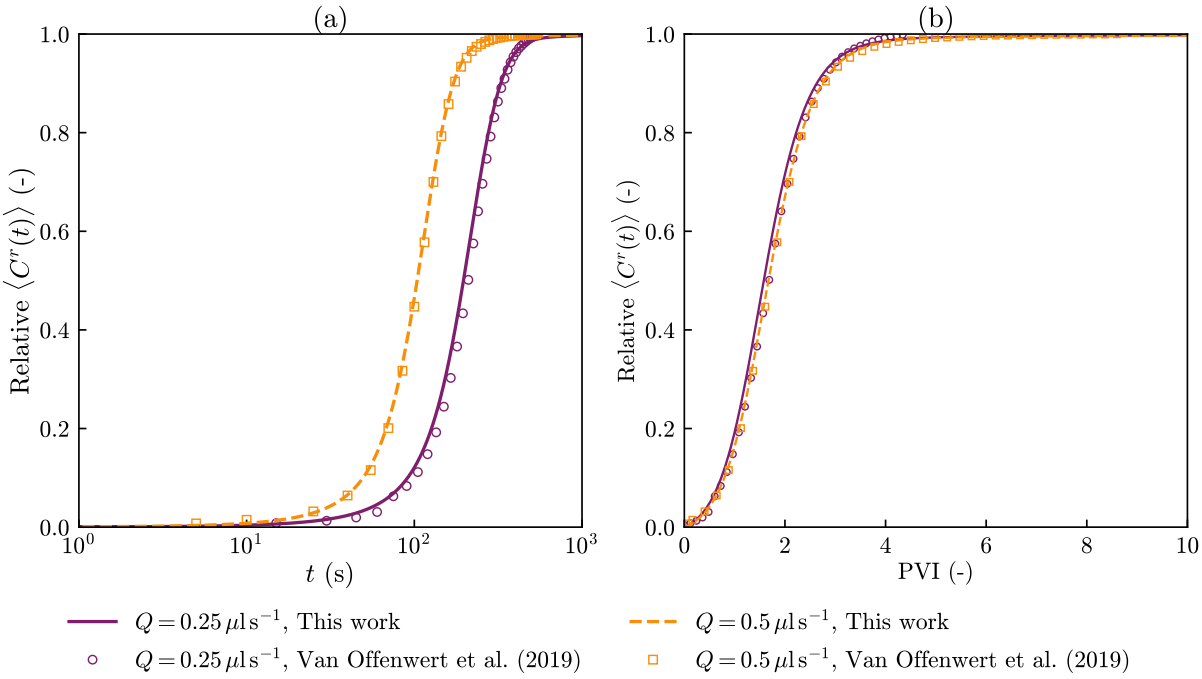

Figure 2: Comparison of relative $\langle C^r \rangle$ obtained numerically (this work) and experimentally (Van Offenwert et al. (2019)) for solute injection rates of 0.25 and 0.50 $\mu l\,s^{-1}$: normalised concentration plotted against (a) time and (b) pore volume injected (PVI = t/t_{ad}).

4. Results and discussion

4.1. Breakthrough curves

Figure 3 illustrates $\langle C^f(t)\rangle$ against PVI at different ΔP and S values for the three pore networks. It is evident that the breakthrough curves transition from non-Fickian behaviour, characterised by pronounced tailing, to more Fickian behaviour as S increases towards unity, irrespective of λ and ΔP. This trend is expected because, at different S values, imposing a constant ΔP results in different flow rates and characteristic velocities, and hence different Pe numbers (Table 2). Similar behaviour has been observed experimentally by Padilla et al. (1999) and numerically by Hasan et al. (2019) and An et al. (2020a), highlighting the critical role of saturation in shaping the magnitude and distribution of the pore-scale velocity field under a given hydrodynamic forcing, thereby governing solute transport dynamics in partially saturated porous media. Figures 4 and 5 show the evolution of the average concentrations in the flowing and stagnant regions, C_f and C_s, as a function of PVI for the same ΔP and S conditions. As expected, concentrations in both regions evolve over time; however, their rates of change differ due to contrasting transport mechanisms. In the flowing region, concentration evolution is

primarily controlled by advection, leading to a rapid increase towards the unity at small PVI. In contrast, transport in the stagnant region is diffusion dominated, resulting in a slower approach. Moreover, the evolution of C_s is non-linear in time, which is consistent with a temporally varying mass transfer rate between the flowing and stagnant regions.

To quantify the role of S in controlling non-Fickian transport, we define τ as the PVI required for $\langle C^f(t)\rangle$ to increase from 0.0 to 0.99 and plot it against S for different λ and ΔP in Figure 6. As observed, τ decreases with increasing S for all λ and ΔP values, consistent with the BTC trends in Figure 3. This declining behaviour is because higher S values provide greater interconnected pore space for the invading fluid flow, and accordingly, solute transport. At lower S, more pores act as dead-ends, reducing hydraulic conductivity, increasing tortuosity, and thereby limiting effective solute transport and promoting non-Fickian behaviour. Furthermore, for a given λ and S, τ generally decreases with increasing ΔP, as higher pressure gradients increase mean and local pore velocities (and thus Pe), accelerating advective transport and reducing the PVI required to reach $\langle C^f(t)\rangle = 0.99$. In addition, for a given ΔP, higher τ values are observed at larger λ. This behaviour reflects the fact that increasing spatial correlation in pore sizes promotes the formation of extended preferential flow pathways coexisting with larger and more persistent low-velocity or stagnant regions. Given these stagnant regions are less efficiently accessed by advective transport and rely predominantly on diffusive mass exchange with the flowing zones, which slows solute equilibration and prolongs late-time tailing in the BTCs. As a result, a larger injected pore volume is required for $\langle C^f(t)\rangle$ to approach unity, leading to increased τ values and more pronounced non-Fickian behaviour (An et al., 2020b). As S approaches unity, the τ values converge across all λ and ΔP cases, indicating that most of the pore space becomes accessible to the solute, thereby reducing non-Fickian transport characterstics. We emphasise that above comparative discussion reflects transport behaviour under two-phase flow conditions in which saturation, pore connectivity, velocity distributions, and Pe are intrinsically coupled.

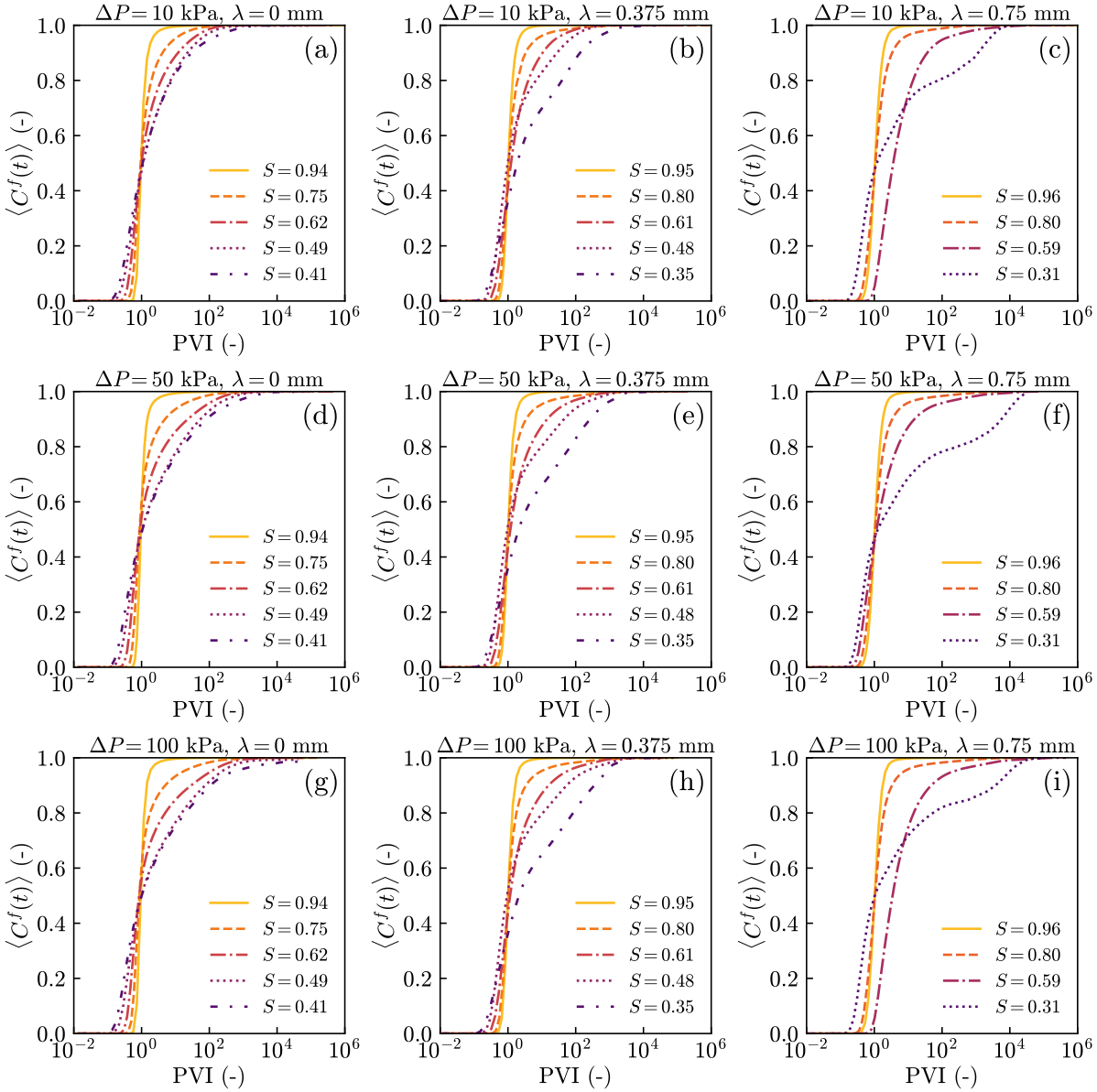

Figure 3: Evolution of $\langle C^f(t) \rangle$ versus PVI at different S, λ, and ΔP values. The corresponding Pe numbers for each case are provided in Table 2.

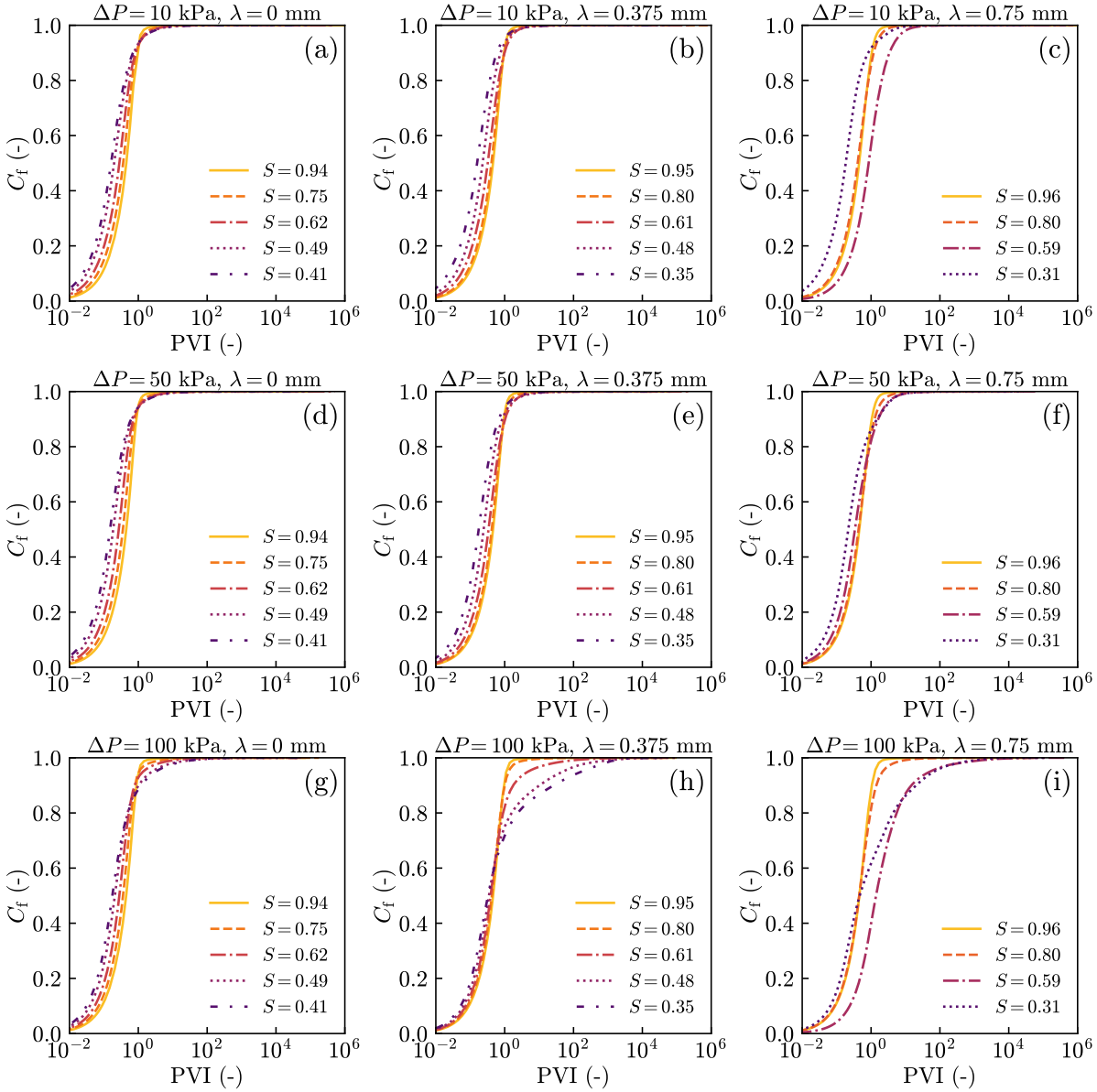

Figure 4: Evolution of C_f versus PVI at different S, λ, and ΔP values.

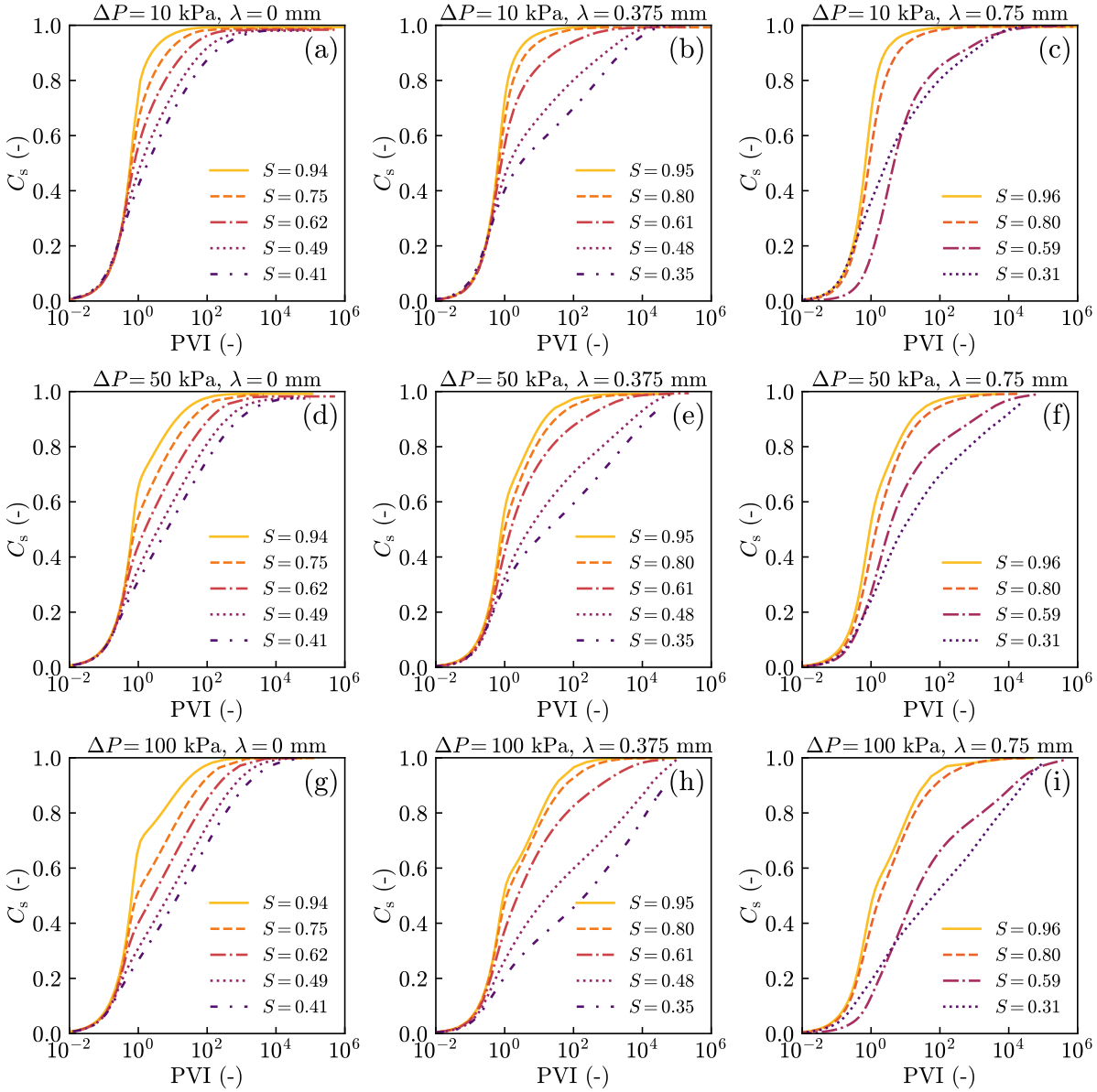

Figure 5: Evolution of C_s versus PVI at different S, λ, and ΔP values.

4.2. Transport properties

In this section, the transport properties estimated via inverse modelling and fitting the BTCs to each transport model will be compared with each other and against the DE. The transport parameters in the MIM and MRMT models and DE include S_s, D, and γ and those in the CTRW model include β, D, and t_2.

4.2.1. Stagnant saturation and transport behaviour

As S_s quantifies stagnant zones (dead-ends, narrow throats, cul-de-sacs) which contribute poorly to flow and transport, its variation is expected to reflect the trends observed

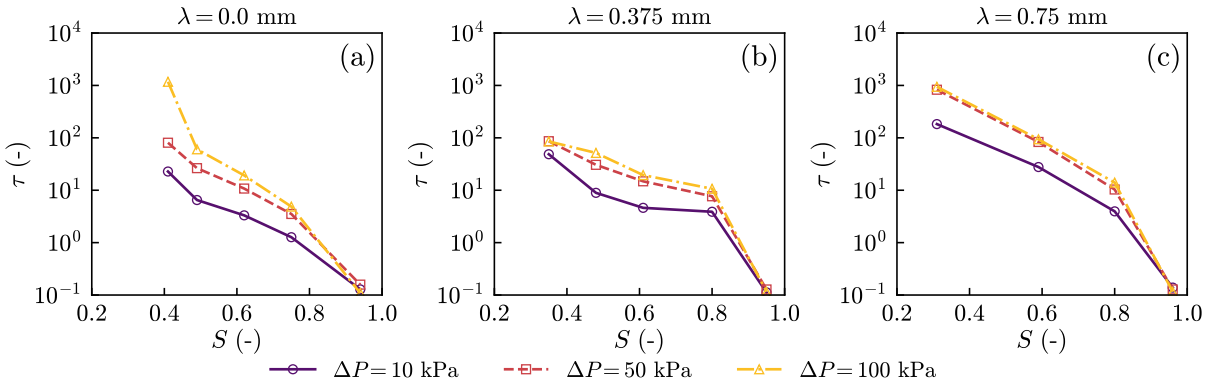

Figure 6: The variation of τ, defined as the PVI required for $\langle C^f(t)\rangle$ to increase from 0.0 to 0.99, versus S at different values of ΔP for the three pore networks.

in the BTCs (section 4.1). Figure 7 presents the values of S_s estimated by the DE as well as MIM and MRMT models as a function of S for the three pore networks at different ΔP values. As observed, the DE estimates a negligible increase in S_s at low S values, followed by a steeper decline as S approaches unity (Figure 7(a-c)), whereas regardless of ΔP and λ, S_s follows a concave trend in the MIM and MRMT models (Figure 7(d-f) and (g-i), respectively). The initial slight increase in S_s estimated by the DE aligns with percolation theory, which suggests that the fraction of dead-end pores reaches its maximum between the percolation threshold and a fully connected network (Hasan et al., 2019). The subsequent decrease at higher S values can be attributed to the increasing presence of interconnected pores. However, the pronounced increase in S_s predicted by the MIM and MRMT models at low to intermediate saturations contradicts the trends observed in Figures 3) and Figure 6. In some cases, this trend may not even be physically meaningful—for example, at $\lambda = 0.0$ mm, $\Delta P = 100$ kPa, and $S = 0.62$, the predicted $S_s = 0.56$ implies $S_f = 0.06$, which is unrealistic. This discrepancy shows that the MIM and MRMT frameworks may not adequately distinguish the contributions of flowing and stagnant zones to fluid flow and solute transport at low and intermediate saturations when fitting the BTC data.

The predicted S_s values in the MIM and MRMT models also show sensitivity to ΔP in all pore networks, whereas the DE estimates values that remain unaffected by hydrodynamic conditions. Sensitivity of S_s to ΔP, i.e. Pe (see Table 2), is unexpected here because solute injection occurs after the steady-state saturation field has been established. This again highlights a key limitation of the MIM and MRMT models — since S_s is deter-

mined exclusively through fitting the solute BTC to the transport models, its prediction is strongly influenced by BTC evolution. As a result, variations in S_s at different ΔP values are observed, even though steady-state saturation conditions require S_s to remain constant. In contrast, the DE distinguishes stagnant regions from flowing zones based on local residence times rather than BTC fitting. This further supports the argument that estimating S_s purely through inverse modelling and BTC fitting to continuum-scale transport models may be insufficient, as noted by Griffioen et al. (1998) and Hasan et al. (2019).

Since the steady-state saturation field and the distribution of dead-end zones are governed by entry capillary pressure, which in turn, depends on pore size distribution and heterogeneity, S_s is expected to vary with λ at fixed ΔP and S (An et al., 2020a; Saeibehrouzi et al., 2024). Figure 7(a-c) confirms that the DE captures this dependence, estimating lower S_s at higher λ. In contrast, while the MIM and MRMT models also yield different S_s values for varying λ, no consistent trend emerges.

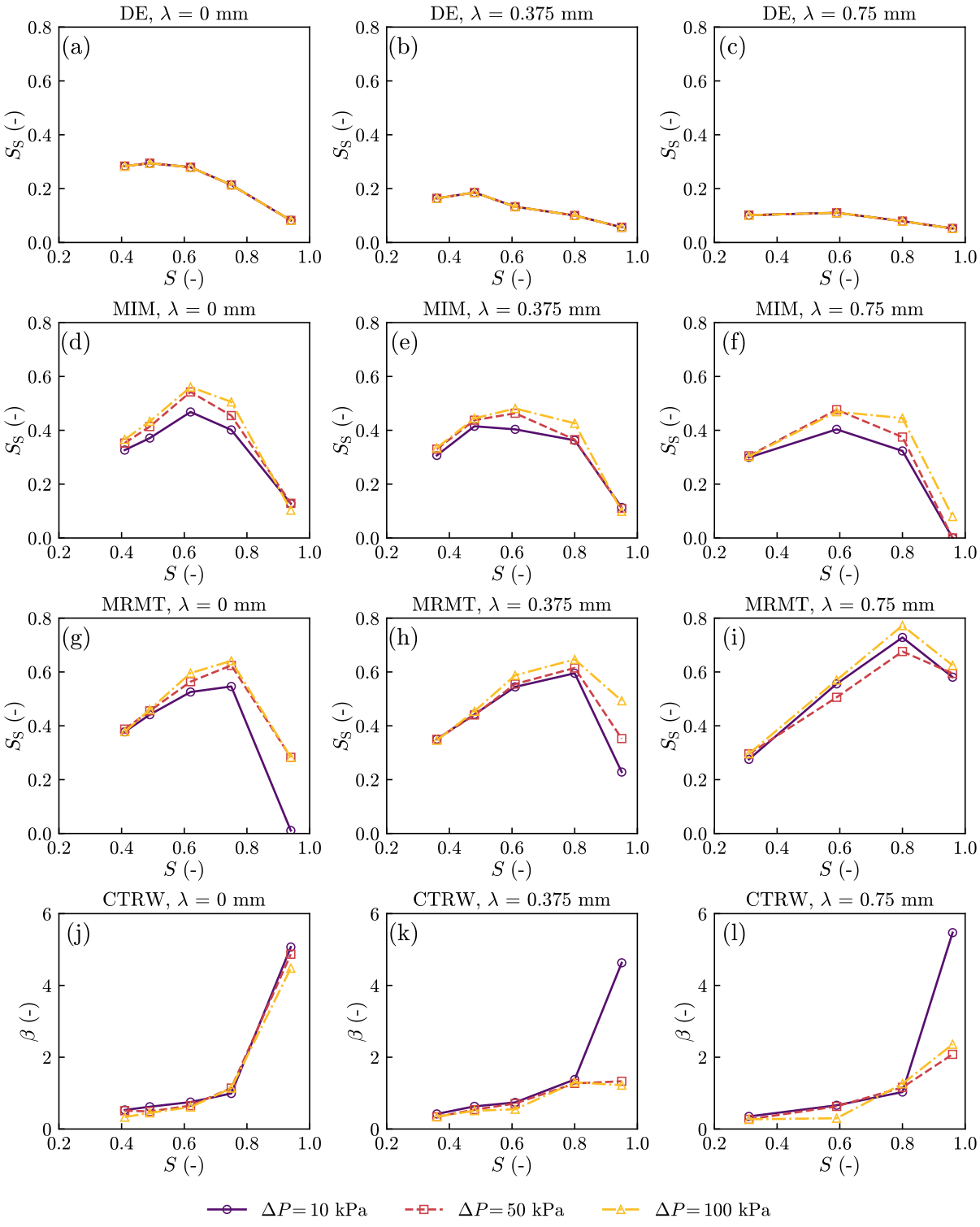

Figure 7: Stagnant saturation (S_s) estimated from the DE and predicted by the MIM and MRMT models, together with β predicted by the CTRW model, plotted against total saturation (S) for various ΔP and λ values; the DE results overlap for different ΔP at a given λ value.

Unlike the other models, the CTRW model does not estimate S_s but instead employs a TPL probability distribution function (Equation (10)) to determine β and characterise

solute transport. Figure 7(j-l) presents β as a function of S for the three pore networks at different ΔP values. As observed, β generally increases with S, indicating a transition toward Fickian transport. This trend is consistent with previous studies (Cortis and Berkowitz, 2004; Cortis and Birkholzer, 2008) and aligns with trends in BTCs (Figure 3) and τ values (Figure 6). At low to intermediate S values, $\beta < 2$ suggests non-Fickian transport with minimal sensitivity to hydrodynamic conditions. However, as S approaches unity, β becomes hydrodynamically dependent. Specifically, for $S > 0.9$, β sharply reaches $\sim$5 at all ΔP values in the uncorrelated pore network (Figure 7(j)), signifying strong Fickian transport. In the correlated pore networks, transport remains strongly Fickian at $\Delta P = 10$ kPa, as reflected by $\beta \gg 2$. At higher ΔP values, although the breakthrough curves at high saturation appear increasingly Fickian (Figure 3), the corresponding CTRW fits yield β values that approach, but do not significantly exceed, $\beta = 2$. This indicates that while the macroscopic BTCs exhibit near-Fickian behaviour, the CTRW framework becomes less sensitive in distinguishing fully Fickian transport once advective transport dominates and residence-time distributions narrow.

4.2.2. Dispersion Coefficient

Figure 8 shows the dispersion coefficient (D) estimates from the DE as well as predictions from the MIM, MRMT, and CTRW models as a function of S for the three pore networks at different ΔP values. Consistent with previous experimental findings (Mohanty and Salter, 1982; Padilla et al., 1999) and in agreement with DE estimates (Figure 8(a-c)), the MIM model predicts a non-monotonic relationship between D and S in all cases, with higher D values at intermediate saturations (Figure 8(d-f)). This behaviour arises from the competing influences of increasing advective transport strength and the evolution of stagnant regions with saturation. At very low S, dispersion remains small because, regardless of S_s, advective transport is highly restricted by low effective permeability and poor phase connectivity, resulting in small Pe (Table 2). As S increases toward intermediate values, additional pores become accessible to the invading phase; consequently, effective permeability and average pore velocity increase, strengthening advective transport (and hence Pe, see Table 2), while preferential flow pathways coexist with stagnant or poorly connected regions. The interaction between fast-moving and slow-moving zones enhances solute spreading, leading to a peak in dispersion. As $S \to 1$, the fraction and influence of stagnant regions decrease substantially (see Figure

554 7). This reduction in mass-exchange contrast between flowing and stagnant zones out-
555 weighs the comparatively modest increase in advective strength, resulting in a decrease
556 in dispersion. This behaviour has also been observed experimentally by Karadimitriou
557 et al. (2017). It can be seen that the MRMT and CTRW models fail to accurately cap-
558 ture this behaviour in most cases, despite successfully predicting the overall range of D
559 variations (Figure 8(g-i) and (j-l), respectively). In the MRMT model, the predicted
560 dispersion reflects the superposition of multiple mass transfer rates associated with a pre-
561 scribed distribution of immobile regions, which can lead to deviations from the physically
562 expected saturation dependence. The inability of the CTRW model to reproduce the non-
563 monotonic dependence of D on saturation stems from its formulation (2.3). The CTRW
564 model does not reproduce the non-monotonic dependence of D on saturation because
565 dispersion in CTRW is controlled by the statistics of particle transition times through
566 the memory function $\tilde{M}(u)$ and TPL probability distribution function $\psi(t)$, rather than
567 by explicit saturation-dependent reorganisation of pore-scale velocity fields. As a result,
568 changes in saturation primarily affect the fitted parameters β and t_2, while the dispersion
569 coefficient D_ψ remains insensitive to the competition between preferential flow pathways
570 and stagnant regions that gives rise to peak dispersion at intermediate saturations.

571 For low to intermediate S and a given ΔP, the MRMT model estimates higher D
572 values than the DE, MIM, and CTRW models, with the CTRW model predicting the
573 lowest D values, even as $S \to 1$. The high dispersion coefficient predicted by the MRMT
574 model in this saturation range is due to its consideration of multiple mass transfer rates
575 from stagnant regions (Equation 4), leading to an overestimation of dispersion, as noted
576 in previous studies (Muniruzzaman and Rolle, 2017; Lu et al., 2018). The low dispersion
577 coefficients predicted by the CTRW model is due to its definition, which is based on the
578 time scale of transport (see Equation (8)), offering a distinct physical interpretation com-
579 pared to the other models (Berkowitz et al., 2006; Berkowitz and Scher, 2009). Although
580 previous studies have not fully explained the physical meaning of the CTRW dispersion
581 coefficient, one study classified the average pore velocity in CTRW as the average parti-
582 cle velocity of a solute particle moving between two pores (Cortis and Berkowitz, 2004).
583 Assuming that D is defined as dispersivity (α) multiplied by pore velocity (v), D in the
584 CTRW model can be interpreted as a particle dispersion coefficient.

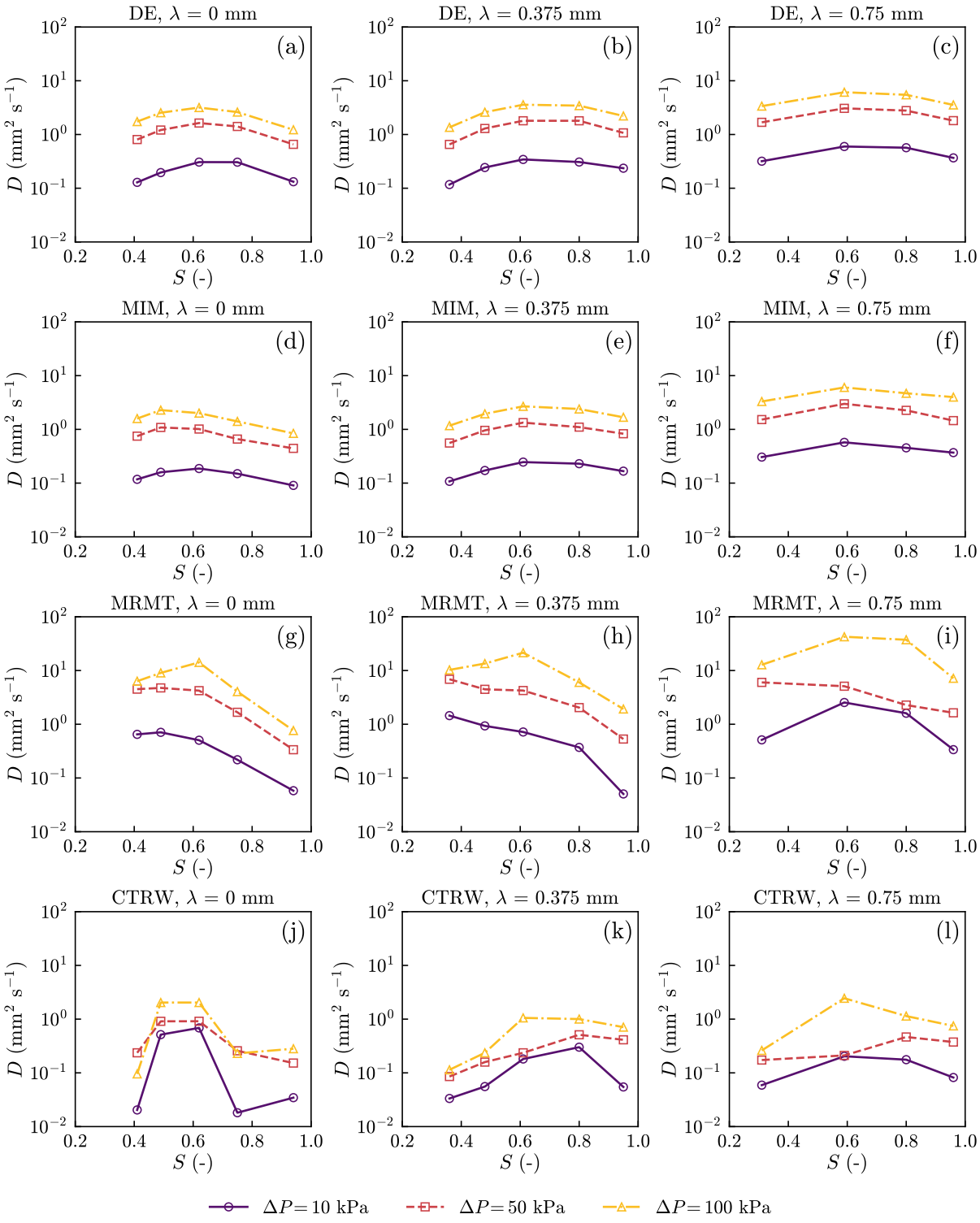

Figure 8: Dispersion coefficient (D) estimated from the DE and predicted by the MIM, MRMT, and CTRW models, plotted against total saturation (S) for various ΔP and λ values.

4.2.3. Mass transfer rate

In this section, we first compare the mass transfer coefficients (γ) estimated by the DE with those predicted by the MIM and MRMT models. The γ values, presented in

Figure 9, are plotted as a function of time at $\Delta P = 100$ kPa and selected S values for the three pore networks. The selected S values are the lowest, intermediate, and highest S values for each pore network in Table 2. Since the trends observed at $\Delta P = 10$ kPa and $\Delta P = 50$ kPa are similar, these results are included in the Supporting Information for brevity.

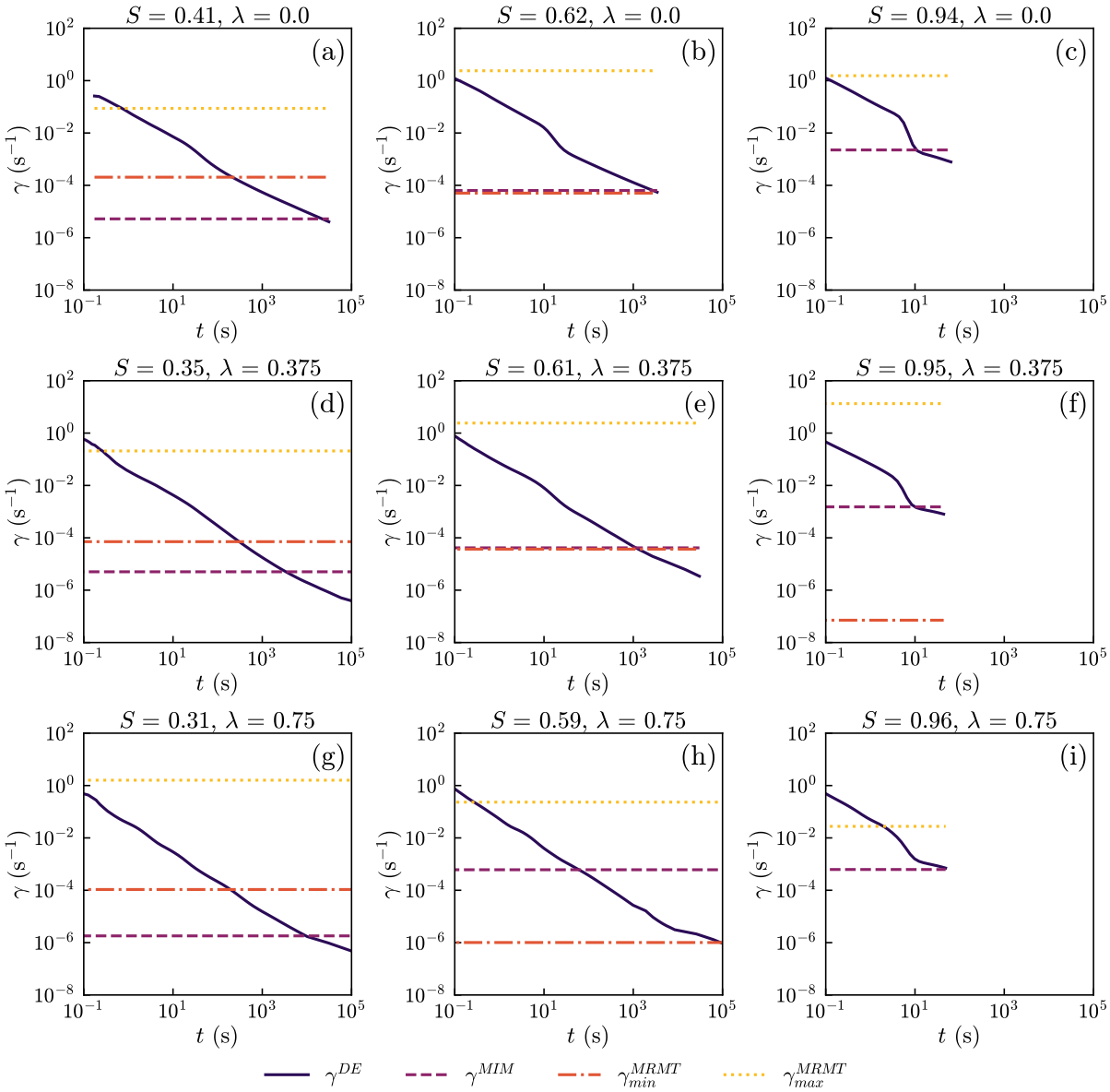

Figure 9: The mass transfer coefficients γ plotted as a function of time at $\Delta P = 100$ kPa and selected S values for the three different pore networks. Note that γ values estimated below 10^{-8} s^{-1} are not shown.

The formulations of γ in different models (see Section 2) inherently require its variability over time, as both the solute concentrations in flowing and stagnant zones and the time derivative of the stagnant concentration evolve due to solute transport and mixing

within the pore space (see Figures 4 and 5).

This behaviour is effectively captured by the DE at different cases, as shown in Figure 9, in agreement with recent modelling and experimental studies (Karadimitriou et al., 2016; An et al., 2020a; Hasan et al., 2019). In contrast, the MIM model predicts a single constant value for γ over time, and the MRMT model estimates a range of constant γ values, with the minimum and maximum values indicated in Figure 9. Although these constant values do not reflect the inherently time-dependent nature of mass transfer between flowing and stagnant zones, they generally fall within the range of time-dependent γ values estimated by DE, thus can be considered as time-averaged approximations and exhibit interesting trends. For instance, at a given λ, the constant γ^{MIM} values generally increase with increasing S. This trend can be attributed to the fact that at higher S, the reduction of S_s enhances mass transfer between stagnant and flowing zones. A similar trend is observed for $\gamma^{MRMT}_{\max}$, except at $\lambda = 0.75$, where a decreasing trend is noted. Meanwhile, $\gamma^{MRMT}_{\min}$ decreases with increasing S, indicating a broader range of γ^{MRMT} values as S increases.

In Figure 9, the time-dependent γ values predicted by the DE follow a power-law decay, $\gamma \propto t^{-\vartheta}$, where ϑ is the correlation exponent. The exponent ϑ was found to range from 0.972 to 1.228 for $\lambda = 0.0$, 1.046 to 1.109 for $\lambda = 0.375$, and 1.052 to 1.119 for $\lambda = 0.75$, indicating a slightly faster decline of γ at higher saturations. However, no clear correlation between ϑ and λ was observed at a given saturation, suggesting that further studies at larger correlation lengths are needed to better understand the impact of heterogeneity on the temporal evolution of γ. The observed power-law behaviour highlights the need to revisit continuum-scale models and to incorporate a time-dependent mass transfer coefficient to more accurately represent solute exchange between flowing and stagnant regions.

As mentioned, the CTRW model does not explicitly estimate the mass transfer rate but instead employs a TPL probability distribution function (Equation (10)) to characterise solute transport by fitting the solute BTC to the CTRW model and obtaining β, t_1, and t_2. Figure 10 presents the temporal evolution of $\langle C^f(t) \rangle$ versus time, along with t_2, at $\Delta P = 100$ kPa and selected S values for the three pore networks. The selected S values correspond to the lowest, intermediate, and highest S values for each pore network in Table 2. Since the trends observed at $\Delta P = 10$ kPa and $\Delta P = 50$ kPa are similar,

these results are included in the Supporting Information for brevity. In Figure 10, it can be seen that t_2 consistently exceeds the final time of the BTC at λ =0.0 and 0.375, in agreement with previous conceptual studies (Dentz and Berkowitz, 2003; Cortis and Berkowitz, 2004), which suggest that t_2 acts as a cutoff time distinguishing transport in the advective-dominated (flowing) zone from that in the diffusion-dominated (stagnant) zone. This is true for low and intermediate saturation cases; however, at high saturation, t_2 is underestimated, indicating that its definition does depend on saturation of the carrying phase. This dependence of t_2 on saturation has been noted by Dentz et al. (2004); Berkowitz et al. (2006), who reported that when the transport time is much greater than t_2, transport behaviour becomes Fickian, whereas when the transport time is much smaller than t_2, transport remains anomalous (non-Fickian).

5. Conclusion

In this work, we investigated non-Fickian solute transport in unsaturated porous media using pore-network modelling under steady-state two-phase flow conditions. Simulations were conducted in three pore networks with different heterogeneity, charactersied by correlation lengths (λ), and differential pressures (ΔP), demonstrating a clear transition from anomalous, long-tailed breakthrough behaviour at low to intermediate saturations to Fickian transport as saturation approaches unity.

A comparative analysis of commonly used continuum-scale models, Mobile-Immobile (MIM), Multirate Mass Transfer (MRMT), and Continuous Time Random Walk (CTRW) was carried out to characterise solute transport properties, and their predictions were compared with each other and against those obtained with the direct estimations (DE). The results showed that the MIM and MRMT, as two traditional inverse modelling approaches, are highly sensitive to the hydrodynamic conditions and, in some cases, yielded physically unrealistic estimates for stagnant saturation (S_s) and mass transfer parameters. The DE, however, consistently captured the expected dependencies on saturation and heterogeneity owing to its use of detailed pore-scale flow and transport information. Moreover, the DE showed a time-dependent mass transfer coefficient (γ), in line with theoretical expectations, whereas the MIM and MRMT models produced constant values that failed to represent the transient dynamics of solute transport.

The CTRW model, as an alternative to traditional approaches, successfully charac-

terised the transition from non-Fickian to Fickian transport with increasing saturation. However, it did not adequately reproduce the non-monotonic variations in dispersion with respect to saturation, a behaviour observed both in our simulations and in available experimental data. While showing some similarities to the MIM and MRMT frameworks, the CTRW model did not fully capture the complex, time-dependent, and heterogeneous features of mass transfer in porous media.

This study demonstrates that commonly used continuum-scale inverse models are fundamentally limited in their ability to infer physically meaningful transport parameters under unsaturated two-phase flow conditions. While such models can reproduce certain macroscopic features of BTCs, their fitted parameters are often sensitive to hydrodynamic conditions, lack physical uniqueness, and do not reliably represent the underlying pore-scale transport mechanisms. As a result, interpreting inverse-model parameters as physically representative quantities can be misleading, particularly in heterogeneous and partially saturated systems. When only breakthrough curve data are available, as is typically the case in field-scale applications, inverse modelling remains a pragmatic but inherently indirect approach. In this context, the present results provide clear guidance on the regimes in which these models are most likely to fail and highlight the risks associated with over-interpreting fitted parameters. The DE, which explicitly incorporates pore-scale velocity fields and residence-time distributions, provides a physically robust basis for quantifying mass transfer, dispersion, and stagnant-zone dynamics. Although its application is currently restricted to systems where detailed pore-scale data are accessible, the insights obtained from DE establish a clear pathway for improving continuum-scale transport models by embedding pore-scale physics rather than relying solely on phenomenological fitting to BTCs.

Taken together, these findings argue for a shift away from purely phenomenological inverse modelling toward hybrid and multiscale approaches that explicitly account for pore-scale heterogeneity and two-phase flow effects. Such a shift is essential for improving predictive reliability in subsurface transport problems, including groundwater contamination, soil remediation, and enhanced oil recovery, where accurate representation of transport processes under partial saturation is critical.

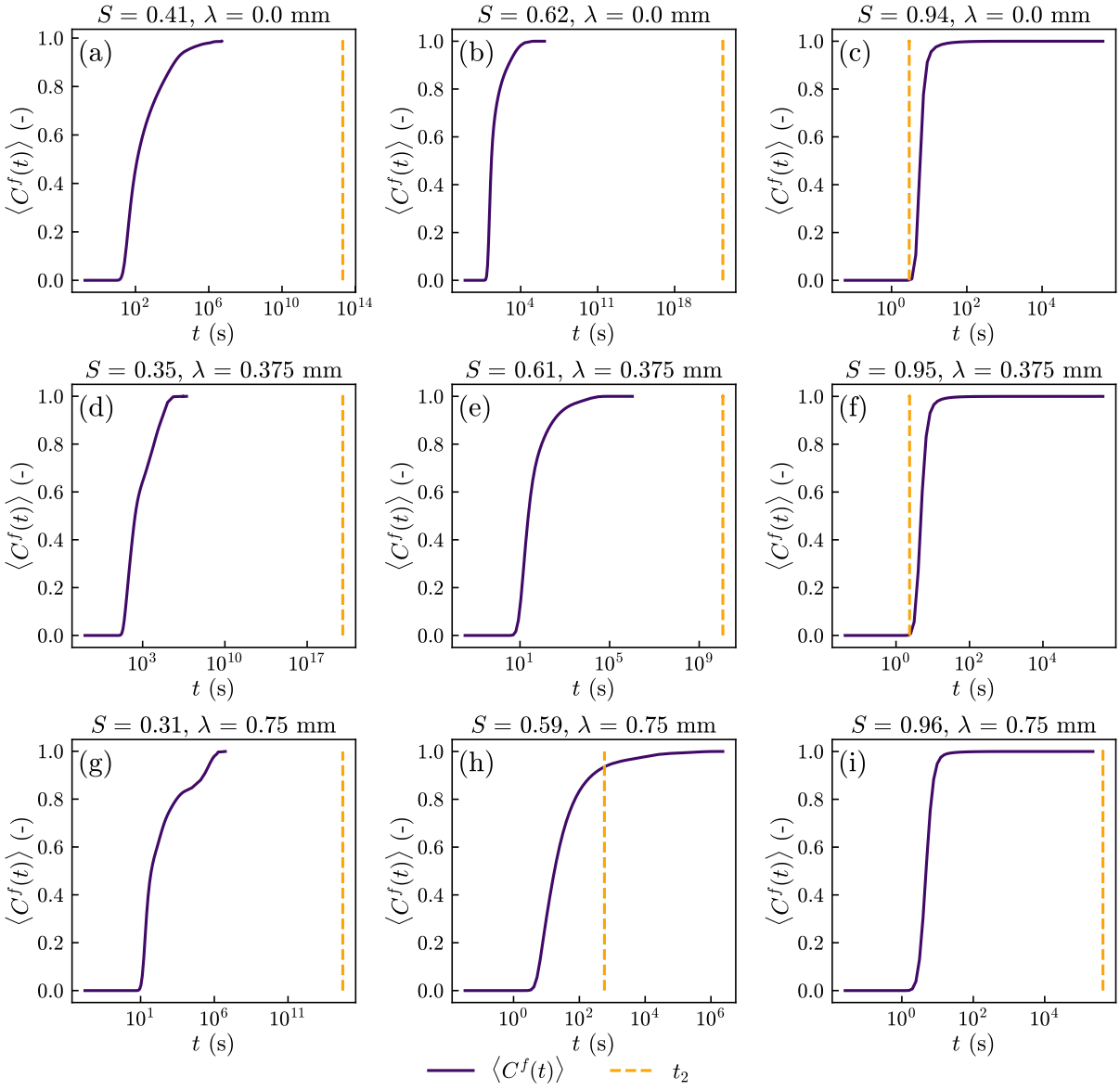

Figure 10: Effluent flux-averaged concentration BTC ($\langle C^f(t) \rangle$) illustrated as solid line, plotted together with t_2, estimated by the CTRW model at $\Delta P = 100$ kPa and selected S values for the three different pore networks.

6. Acknowledgments

SH thanks the Malaysia Ministry of Higher Education and Universiti Teknologi Malaysia [funding reference KPT(BS) 8910271]. MVF was funded by Engineering and Physical Sciences Research Council (EPSRC) PINCH project, EP/W008718/1.

7. Supporting Information

The following are available in the supporting information file: (i) the averaged resident concentration at the inlet, (ii) the breakthrough curves plotted versus time, (iii) the coefficient of determination (R^2) values obtained from fitting the DE and MIM, MRMT, and CTRW models, (iv) mass transfer coefficients at $\Delta P = 10$ kPa and $\Delta P = 50$ kPa, and (v) the temporal evolution of breakthrough curves with t_2.

8. Declaration of Interests

The authors report no conflict of interest.

9. Data Availability Statement

The data that support the findings of this study are available from the corresponding author upon reasonable request.

References

Al-Azani, K., Abu-Khamsin, S., Al-Abdrabalnabi, R., Kamal, M. S., Patil, S., Zhou, X., Hussain, S. M. S., and Al Shalabi, E. (2022). Oil recovery performance by surfactant flooding: a perspective on multiscale evaluation methods. *Energy & Fuels*, 36(22):13451–13478.

Amin, M. H. G., Gibbs, S. J., Chorley, R. J., Richards, K. S., Carpenter, T. A., and Hall, L. D. (1997). Study of flow and hydrodynamic dispersion in a porous medium using pulsed–field–gradient magnetic resonance. *Proceedings of the Royal Society of London. Series A: Mathematical, Physical and Engineering Sciences*, 453(1958):489–513.

An, S., Erfani, H., Godinez-Brizuela, O. E., and Niasar, V. (2020a). Transition from viscous fingering to capillary fingering: Application of gpu-based fully implicit dynamic pore network modeling. *Water Resources Research*, 56(12):e2020WR028149.

An, S., Hasan, S., Erfani, H., Babaei, M., and Niasar, V. (2020b). Unravelling effects of the pore-size correlation length on the two-phase flow and solute transport properties: Gpu-based pore-network modeling. *Water Resources Research*, 56(8):e2020WR027403.

Aziz, R., Joekar-Niasar, V., and Martinez-Ferrer, P. (2018). Pore-scale insights into transport and mixing in steady-state two-phase flow in porous media. *International Journal of Multiphase Flow*, 109:51–62.

Babaei, M. and Islam, A. (2018). Convective-reactive co2 dissolution in aquifers with mass transfer with immobile water. *Water Resources Research*, 54(11):9585–9604.

Babaei, M. and Joekar-Niasar, V. (2016). A transport phase diagram for pore-level correlated porous media. *Advances in Water Resources*, 92:23–29.

Baker, L. E. (1977). Effects of dispersion and dead-end pore volume in miscible flooding. *Society of Petroleum Engineers Journal*, 17(03):219–227.

Bello, M. S., Rezzonico, R., and Righetti, P. G. (1994). Use of taylor-aris dispersion for measurement of a solute diffusion coefficient in thin capillaries. *Science*, 266(5186):773–776.

Ben-Noah, I., Hidalgo, J. J., Jimenez-Martinez, J., and Dentz, M. (2023). Solute trapping and the mechanisms of non-fickian transport in partially saturated porous media. *Water Resources Research*, 59(2):e2022WR033613.

Berkowitz, B., Cortis, A., Dentz, M., and Scher, H. (2006). Modeling non-fickian transport in geological formations as a continuous time random walk. *Reviews of Geophysics*, 44(2).

Berkowitz, B., Cortis, A., Dror, I., and Scher, H. (2009). Laboratory experiments on dispersive transport across interfaces: The role of flow direction. *Water Resources Research*, 45(2).

Berkowitz, B., Emmanuel, S., and Scher, H. (2008). Non-fickian transport and multiple-rate mass transfer in porous media. *Water Resources Research*, 44(3).

Berkowitz, B. and Scher, H. (2009). Exploring the nature of non-fickian transport in laboratory experiments. *Advances in Water Resources*, 32(5):750–755.

Biggar, J. W. and Nielsen, D. R. (1960). Diffusion effects in miscible displacement occurring in saturated and unsaturated porous materials. *Journal of Geophysical Research*, 65(9):2887–2895.

Bijeljic, B., Raeini, A., Mostaghimi, P., and Blunt, M. J. (2013). Predictions of non-fickian solute transport in different classes of porous media using direct simulation on pore-scale images. *Physical Review E*, 87(1):013011.

Bromly, M. and Hinz, C. (2004). Non-fickian transport in homogeneous unsaturated repacked sand. *Water Resources Research*, 40(7).

Capuani, F., Frenkel, D., and Lowe, C. P. (2003). Velocity fluctuations and dispersion in a simple porous medium. *Phys. Rev. E*, 67:056306.

Chen, R., Ge, Y., Chen, Z., Liu, J., Zhao, Y., and Li, Z. (2019). Analytical solution for one-dimensional contaminant diffusion through unsaturated soils beneath geomembrane. *Journal of Hydrology*, 568:260–274.

Coats, K. H. and Smith, B. D. (1964). Dead-end pore volume and dispersion in porous media. *Society of Petroleum Engineers Journal*, 4(01):73–84.

Cortis, A. and Berkowitz, B. (2004). Anomalous transport in "classical" soil and sand columns. *Soil Science Society of America Journal*, 68(5):1539–1548.

Cortis, A. and Birkholzer, J. (2008). Continuous time random walk analysis of solute transport in fractured porous media. *Water Resources Research*, 44(6).

Cortis, A., Emmanuel, S., Rubin, S., Willbrand, K., Ben-Zvi, R., and Nissan, A. (2017). The ctrw matlab toolbox v4.0. *Department of Earth and Planetary Sciences*, Weizmann Institute of Science(Wiezmann):Rehovot, Israel.

Dentz, M. and Berkowitz, B. (2003). Transport behavior of a passive solute in continuous time random walks and multirate mass transfer. *Water Resources Research*, 39(5).

Dentz, M., Cortis, A., Scher, H., and Berkowitz, B. (2004). Time behavior of solute transport in heterogeneous media: transition from anomalous to normal transport. *Advances in Water Resources*, 27(2):155–173.

Dong, H. and Blunt, M. J. (2009). Pore-network extraction from micro-computerized-tomography images. *Physical Review E*, 80(3):036307. PRE.

Dou, Z., Tang, S., Zhang, X., Liu, R., Zhuang, C., Wang, J., Zhou, Z., and Xiong, H. (2021). Influence of shear displacement on fluid flow and solute transport in a 3d rough fracture. *Lithosphere*, 2021(Special 4).

Erfani, H., Joekar-Niasar, V., and Farajzadeh, R. (2019). Impact of microheterogeneity on upscaling reactive transport in geothermal energy. *ACS Earth and Space Chemistry*, 3(9):2045–2057.

Fallico, C. (2012). Solute dispersion in porous media at different transport velocities and distances. *International water technology journal.*, 2(2):100.

Gao, G., Feng, S., Zhan, H., Huang, G., and Mao, X. (2009a). Evaluation of anomalous solute transport in a large heterogeneous soil column with mobile-immobile model. *Journal of Hydrologic Engineering*, 14(9):966–974.

Gao, G., Zhan, H., Feng, S., Huang, G., and Mao, X. (2009b). Comparison of alternative models for simulating anomalous solute transport in a large heterogeneous soil column. *Journal of Hydrology*, 377(3):391–404.

Griffioen, J. W., Barry, D. A., and Parlange, J. Y. (1998). Interpretation of two-region model parameters. *Water Resources Research*, 34(3):373–384.

Haggerty, R. (2009). Stammt-l: Solute transport and multirate mass transfer - linear. https://sites.science.oregonstate.edu/~haggertr/STAMMTL/. A solute transport code for multirate mass transfer and reaction along flowlines.

Haggerty, R. and Gorelick, S. M. (1995). Multiple-rate mass transfer for modeling diffusion and surface reactions in media with pore-scale heterogeneity. *Water Resources Research*, 31(10):2383–2400.

Haggerty, R. and Gorelick, S. M. (1998). Modeling mass transfer processes in soil columns with pore-scale heterogeneity. *Soil Science Society of America Journal*, 62(1):62–74.

Haggerty, R., McKenna, S. A., and Meigs, L. C. (2000). On the late-time behavior of tracer test breakthrough curves. *Water Resources Research*, 36(12):3467–3479.

Hasan, S., Joekar-Niasar, V., Karadimitriou, N. K., and Sahimi, M. (2019). Saturation dependence of non-fickian transport in porous media. *Water Resources Research*, 55(2):1153–1166.

Hasan, S., Niasar, V., Karadimitriou, N. K., Godinho, J. R. A., Vo, N. T., An, S., Rabbani, A., and Steeb, H. (2020). Direct characterization of solute transport in unsaturated porous media using fast x-ray synchrotron microtomography. *Proceedings of the National Academy of Sciences*, 117(38):23443–23449.

Hekmatzadeh, M., Dadvar, M., and Sahimi, M. (2016). Pore-network simulation of unstable miscible displacements in porous media. *Transport in Porous Media*, 113(3):511–529.

Huysmans, M. and Dassargues, A. (2005). Review of the use of péclet numbers to determine the relative importance of advection and diffusion in low permeability environments. *Hydrogeology Journal*, 13(5):895–904.

Jiménez-Martinez, J., Le Borgne, T., Tabuteau, H., and Méheust, Y. (2017). Impact of saturation on dispersion and mixing in porous media: Photobleaching pulse injection experiments and shear-enhanced mixing model. *Water Resources Research*, 53(2):1457–1472.

Karadimitriou, N. K., Joekar-Niasar, V., Babaei, M., and Shore, C. A. (2016). Critical role of the immobile zone in non-fickian two-phase transport: A new paradigm. *Environmental Science & Technology*, 50(8):4384–4392.

Karadimitriou, N. K., Joekar-Niasar, V., and Brizuela, O. G. (2017). Hydro-dynamic solute transport under two-phase flow conditions. *Scientific Reports*, 7(1):6624.

Leharne, S. (2019). Transfer phenomena and interactions of non-aqueous phase liquids in soil and groundwater. *ChemTexts*, 5(1):5.

Li, Y., Farrher, G., and Kimmich, R. (2006). Sub-and superdiffusive molecular displacement laws in disordered porous media probed by nuclear magnetic resonance. *Physical Review E—Statistical, Nonlinear, and Soft Matter Physics*, 74(6):066309.

Lima, R., Ishikawa, T., Imai, Y., Takeda, M., Wada, S., and Yamaguchi, T. (2008). Radial dispersion of red blood cells in blood flowing through glass capillaries: The role of hematocrit and geometry. *Journal of Biomechanics*, 41(10):2188–2196.

Liu, Y., Xiao, H., Aquino, T., Dentz, M., and Wang, M. (2024). Scaling laws and mechanisms of hydrodynamic dispersion in porous media. *Journal of Fluid Mechanics*, 1001:R2.

Lu, B., Zhang, Y., Zheng, C., Green, T. C., O'Neill, C., Sun, H.-G., and Qian, J. (2018). Comparison of time nonlocal transport models for characterizing non-fickian transport: From mathematical interpretation to laboratory application. *Water*, 10(6).

Mahmoodlu, M. G., Raoof, A., Bultreys, T., Van Stappen, J., and Cnudde, V. (2020). Large-scale pore network and continuum simulations of solute longitudinal dispersivity of a saturated sand column. *Advances in Water Resources*, 144:103713.

Maraqa, M. A., B. Wallace, R., and C. Voice, T. (1997). Effects of degree of water saturation on dispersivity and immobile water in sandy soil columns. *Journal of Contaminant Hydrology*, 25(3):199–218.

Mineo, S. (2023). Groundwater and soil contamination by lnapl: State of the art and future challenges. *Science of The Total Environment*, 874:162394.

Mohanty, K. K. and Salter, S. J. (1982). Multiphase flow in porous media: Ii. pore-level modeling. In *SPE Annual Technical Conference and Exhibition*, pages SPE–11018–MS. Society of Petroleum Engineers.

Muniruzzaman, M. and Rolle, M. (2017). Experimental investigation of the impact of compound-specific dispersion and electrostatic interactions on transient transport and solute breakthrough. *Water Resources Research*, 53(2):1189–1209.

Ogata, A. and Banks, R. B. (1961). *A solution of the differential equation of longitudinal dispersion in porous media: fluid movement in earth materials*. US Government Printing Office.

Padilla, I. Y., Yeh, T. J., and Conklin, M. H. (1999). The effect of water content on solute transport in unsaturated porous media. *Water Resources Research*, 35(11):3303–3313.

Raeini, A. Q., Bijeljic, B., and Blunt, M. J. (2017). Generalized network modeling: Network extraction as a coarse-scale discretization of the void space of porous media. *Physical Review E*, 96(1):013312.

Raoof, A. and Hassanizadeh, S. M. (2013). Saturation-dependent solute dispersivity in porous media: Pore-scale processes. *Water Resources Research*, 49(4):1943–1951.

Saeibehrouzi, A., Holtzman, R., Denissenko, P., and Abolfathi, S. (2024). Solute transport in unsaturated porous media with spatially correlated disorder. *Advances in Water Resources*, 191:104773.

Saffman, P. G. (1959). A theory of dispersion in a porous medium. *Journal of Fluid Mechanics*, 6(3):321–349.

Sahimi, M. (1993). Nonlinear transport processes in disordered media. *AIChE Journal*, 39(3):369–386.

Scher, H. and Lax, M. (1973). Stochastic transport in a disordered solid. i. theory. *Phys. Rev. B*, 7:4491–4502.

Singh, K. and Obi, V. (2025). Péclet number and transport length dependences of dispersion and dispersivity coefficients during the transition to fickian transport in homogeneous sands. *Advances in Water Resources*, 200:104975.

Souzy, M., Lhuissier, H., Méheust, Y., Le Borgne, T., and Metzger, B. (2020). Velocity distributions, dispersion and stretching in three-dimensional porous media. *Journal of Fluid Mechanics*, 891:A16.

Su, N. (2012). Distributed-order infiltration, absorption and water exchange in mobile and immobile zones of swelling soils. *Journal of Hydrology*, 468-469:1–10.

Tecklenburg, J., Neuweiler, I., Carrera, J., and Dentz, M. (2016). Multi-rate mass transfer modeling of two-phase flow in highly heterogeneous fractured and porous media. *Advances in Water Resources*, 91:63–77.

Toride, N., Inoue, M., and Leij, F. J. (2003). Hydrodynamic dispersion in an unsaturated dune sand. *Soil Science Society of America Journal*, 67(3):703–712.

Toride, N., Leij, L., and van Genuchten, M. T. (1995). he cxtfit code for estimating transport parameters from laboratory or field tracer experiments. version 2.0. *Research Report No. 137*, U. S. Salinity Laboratory(USDA):ARS, Riverside, CA.

Valvatne, P. H. and Blunt, M. J. (2004). Predictive pore-scale modeling of two-phase flow in mixed wet media. *Water Resources Research*, 40(7).

Van Genuchten, M. T., Šimunek, J., Leij, F., Toride, N., and Šejna, M. (2012). Stanmod: Model use, calibration, and validation. *Transactions of the ASABE*, 55(4):1355–1366.

van Genuchten, M. T. and Wierenga, P. J. (1976). Mass transfer studies in sorbing porous media i. analytical solutions1. *Soil Science Society of America Journal*, 40(4):473–480.

Van Offenwert, S., Cnudde, V., and Bultreys, T. (2019). Pore-scale visualization and quantification of transient solute transport using fast microcomputed tomography. *Water Resources Research*, 55(11):9279–9291.

Van Offenwert, S., Cnudde, V., Ellman, S., and Bultreys, T. (2024). Direct pore-scale comparison of solute transport in saturated and unsaturated porous media using fast micro-computed tomography. *Transport in Porous Media*, 151(10):2017–2039.

Velásquez-Parra, A., Aquino, T., Willmann, M., Méheust, Y., Le Borgne, T., and Jiménez-Martínez, J. (2022). Sharp transition to strongly anomalous transport in unsaturated porous media. *Geophysical Research Letters*, 49(3):e2021GL096280.

Wang, Q., Bian, J., Wan, H., and Gu, T. (2019). Non-fickian transport of ammonia nitrogen in vadose zone: experiments and modeling. *Arabian Journal of Geosciences*, 12(23):711.

Yoon, S. and Kang, P. K. (2021). Roughness, inertia, and diffusion effects on anomalous transport in rough channel flows. *Phys. Rev. Fluids*, 6:014502.

Zhang, C., Suekane, T., Minokawa, K., Hu, Y., and Patmonoaji, A. (2019). Solute transport in porous media studied by lattice boltzmann simulations at pore scale and x-ray tomography experiments. *Phys. Rev. E*, 100:063110.

Zhuang, L., Raoof, A., Mahmoodlu, M. G., Biekart, S., de Witte, R., Badi, L., van Genuchten, M. T., and Lin, K. (2021). Unsaturated flow effects on solute transport in porous media. *Journal of Hydrology*, 598:126301.

Zoia, A., Néel, M.-C., and Cortis, A. (2010). Continuous-time random-walk model of transport in variably saturated heterogeneous porous media. *Physical Review E*, 81(3):031104.

Supporting Information for

Comparative Evaluation of Models for Non-Fickian Transport in Unsaturated Porous Media

Sharul Hasan[†,a,b], Mehrdad Vasheghani Farahani[†,b], Stefanie Van Offenwert[c], Tom Bultreys[c], Vahid Niasar[*,b]

[*] *Corresponding author: vahid.niasar@manchester.ac.uk*

[†] *S.H and M.V.F have equally contributed to this article.*

[a] *Department of Petroleum Engineering, Faculty of Chemical and Energy Engineering, Universiti Teknologi Malaysia, 81310 Johor Bahru, Johor, Malaysia*

[b] *Department of Chemical Engineering, University of Manchester, Oxford Road, Manchester, M13 9PL, UK*

[c] *Pore-scale Processes in Geomaterials Research Group (PProGRess), Department of Geology, Ghent University, Krijgslaan 281 S8, 9000 Ghent, Belgium*

Figure S1 presents the averaged resident concentration ($C(t)|_{in}$) at the inlet, derived from data in a previous study (Van Offenwert et al., 2019), and used to estimate parameters a and b in Equation (20) via curve fitting. The obtained values were $a = 0.0359$ and $b = 107.5077$ for the injection rate of 0.25 μl s^{-1}, and $a = 0.0186$ and $b = 211.4801$ for 0.50 μl s^{-1}.

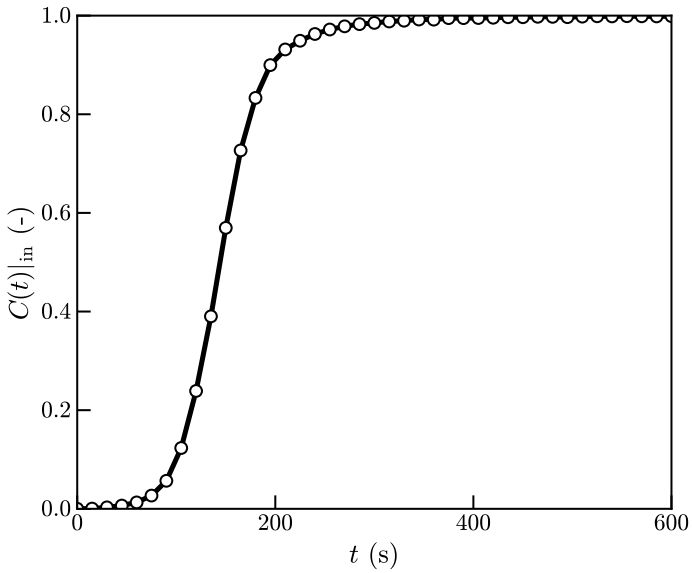

Figure S1: Averaged resident concentration at the inlet. The dataset was obtained from Van Offenwert et al. (2019).

Figure S2 shows the evolution of $\langle C^f(t)\rangle$ versus time at different λ and ΔP values.

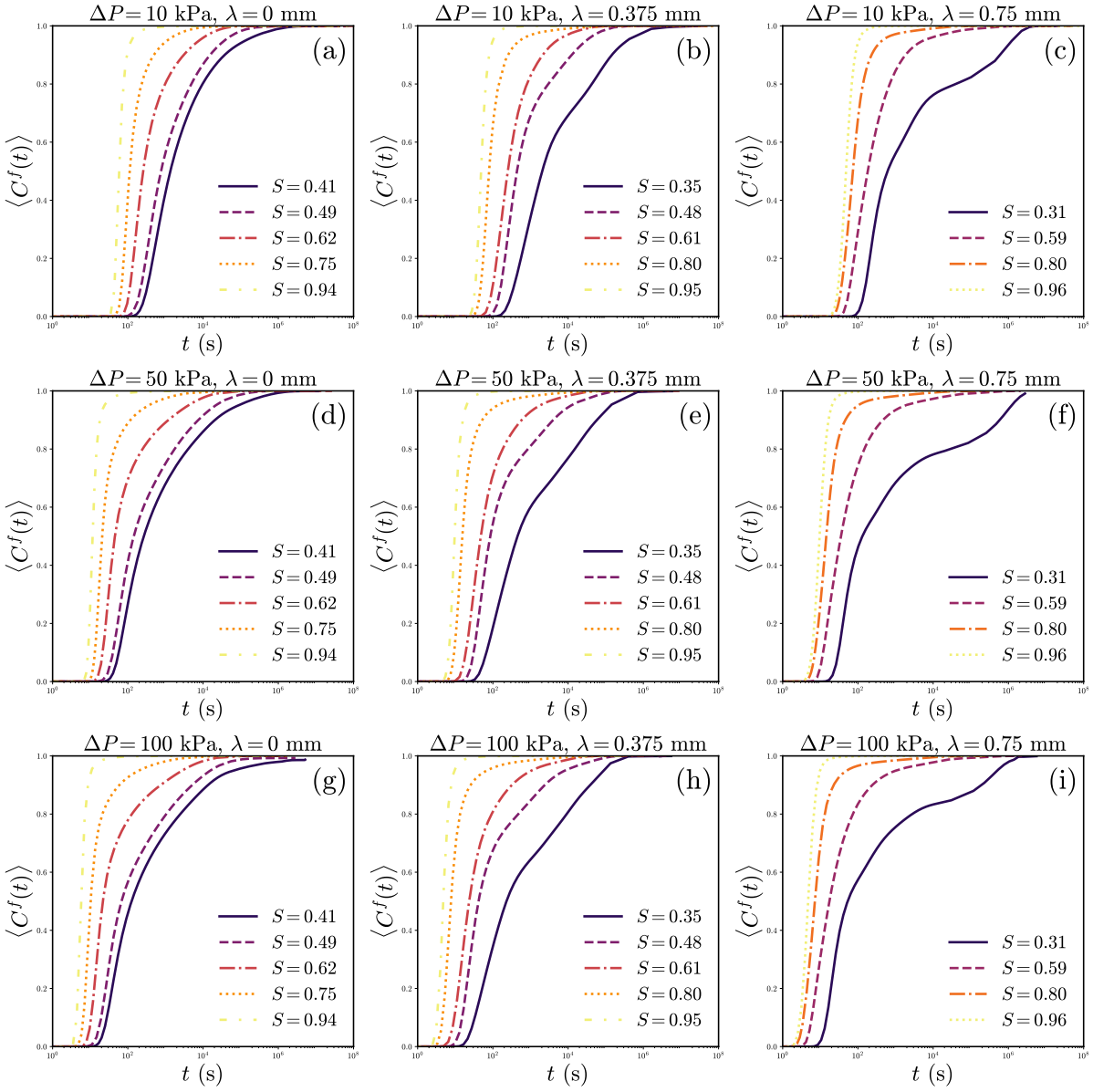

Figure S2: Evolution of $\langle C^f(t)\rangle$ versus time (t) at different λ and ΔP values.

Tables S1, S2, S3, and S4 present the coefficient of determination (R^2) values obtained from fitting the DE and MIM, MRMT, and CTRW models, respectively, to the effluent flux-averaged concentration breakthrough curves ($\langle C^f(t)\rangle$) for all the simulation cases.

Table S1: R^2 values for the DE fitted to the effluent flux-averaged concentration breakthrough curves.

R^2 for uncorrelated network ($\lambda = 0.0$ mm)

ΔP (kPa)	$S = 0.41$	$S = 0.49$	$S = 0.62$	$S = 0.75$	$S = 0.94$
10	0.9975	0.9956	0.9828	0.9823	0.9964
50	0.9952	0.9918	0.9744	0.9739	0.9961
100	0.9937	0.9890	0.9674	0.9750	0.9978

R^2 for correlated network ($\lambda = 0.375$ mm)

ΔP (kPa)	$S = 0.35$	$S = 0.48$	$S = 0.61$	$S = 0.80$	$S = 0.95$
10	0.9931	0.9822	0.9893	0.9942	0.9987
50	0.9972	0.9799	0.9881	0.9901	0.9990
100	0.9968	0.9779	0.9871	0.9907	0.9989

R^2 for correlated network ($\lambda = 0.75$ mm)

ΔP (kPa)	$S = 0.31$	$S = 0.59$	$S = 0.80$	$S = 0.96$
10	0.9872	0.9955	0.9965	0.9996
50	0.9829	0.9940	0.9965	0.9996
100	0.9810	0.9936	0.9970	0.9997

Table S2: R^2 values for the MIM model fitted to the effluent flux-averaged concentration breakthrough curves.

R^2 for uncorrelated network ($\lambda = 0.0$ mm)

ΔP (kPa)	$S = 0.41$	$S = 0.49$	$S = 0.62$	$S = 0.75$	$S = 0.94$
10	0.9981	0.9985	0.9978	0.9985	0.9999
50	0.9984	0.9988	0.9952	0.9992	0.9999
100	0.9956	0.9946	0.9942	0.9973	0.9998

R^2 for correlated network ($\lambda = 0.375$ mm)

ΔP (kPa)	$S = 0.35$	$S = 0.48$	$S = 0.61$	$S = 0.80$	$S = 0.95$
10	0.9978	0.9980	0.9989	0.9993	0.9990
50	0.9976	0.9968	0.9978	0.9989	0.9990
100	0.9946	0.9960	0.9975	0.9985	0.9990

R^2 for correlated network ($\lambda = 0.75$ mm)

ΔP (kPa)	$S = 0.31$	$S = 0.59$	$S = 0.80$	$S = 0.96$
10	0.9931	0.9981	0.9997	0.9995
50	0.9878	0.9894	0.9995	0.9990
100	0.9885	0.9971	0.9994	0.9996

Table S3: R^2 values for the MRMT model fitted to the effluent flux-averaged concentration breakthrough curves.

R^2 for uncorrelated network ($\lambda = 0.0$ mm)

ΔP (kPa)	$S = 0.41$	$S = 0.49$	$S = 0.62$	$S = 0.75$	$S = 0.94$
10	0.9875	0.9990	0.9998	0.9990	0.9990
50	0.9990	0.9998	0.9999	0.9990	0.9990
100	0.9998	0.9999	0.9999	0.9990	0.9990

R^2 for correlated network ($\lambda = 0.375$ mm)

ΔP (kPa)	$S = 0.35$	$S = 0.48$	$S = 0.61$	$S = 0.80$	$S = 0.95$
10	0.9983	0.9997	0.9990	0.9995	0.9990
50	0.9973	0.9997	0.9999	0.9990	0.9996
100	0.9970	0.9997	0.9999	0.9999	0.9995

R^2 for correlated network ($\lambda = 0.75$ mm)

ΔP (kPa)	$S = 0.31$	$S = 0.59$	$S = 0.80$	$S = 0.96$
10	0.9962	0.9999	0.9998	0.9990
50	0.9914	0.9998	0.9996	0.9990
100	0.9977	0.9998	0.9996	0.9987

Table S4: R^2 values for the CTRW model fitted to the effluent flux-averaged concentration breakthrough curves.

R^2 for uncorrelated network ($\lambda = 0.0$ mm)

ΔP (kPa)	$S = 0.41$	$S = 0.49$	$S = 0.62$	$S = 0.75$	$S = 0.94$
10	0.9992	0.9975	0.9915	0.9969	0.9966
50	0.9885	0.9947	0.9846	0.9848	0.9958
100	0.9965	0.9940	0.9868	0.9889	0.9975

R^2 for correlated network ($\lambda = 0.375$ mm)

ΔP (kPa)	$S = 0.35$	$S = 0.48$	$S = 0.61$	$S = 0.80$	$S = 0.95$
10	0.9956	0.9925	0.9994	0.9897	0.9983
50	0.9944	0.9909	0.9980	0.9954	0.9986
100	0.9935	0.9902	0.9972	0.9959	0.9994

R^2 for correlated network ($\lambda = 0.75$ mm)

ΔP (kPa)	$S = 0.31$	$S = 0.59$	$S = 0.80$	$S = 0.96$
10	0.9640	0.9995	0.9995	0.9994
50	0.9591	0.9991	0.9986	0.9995
100	0.9714	0.9917	0.9982	0.9998

Figures S3 and S4 present the mass transfer coefficients (γ) estimated by the DE as well as the MIM and MRMT models at $\Delta P = 10$ kPa and $\Delta P = 50$ kPa, respectively, for selected saturation (S) values in the three pore networks (uncorrelated $\lambda = 0.0$ mm, correlated $\lambda = 0.375$ mm, and correlated $\lambda = 0.75$ mm).

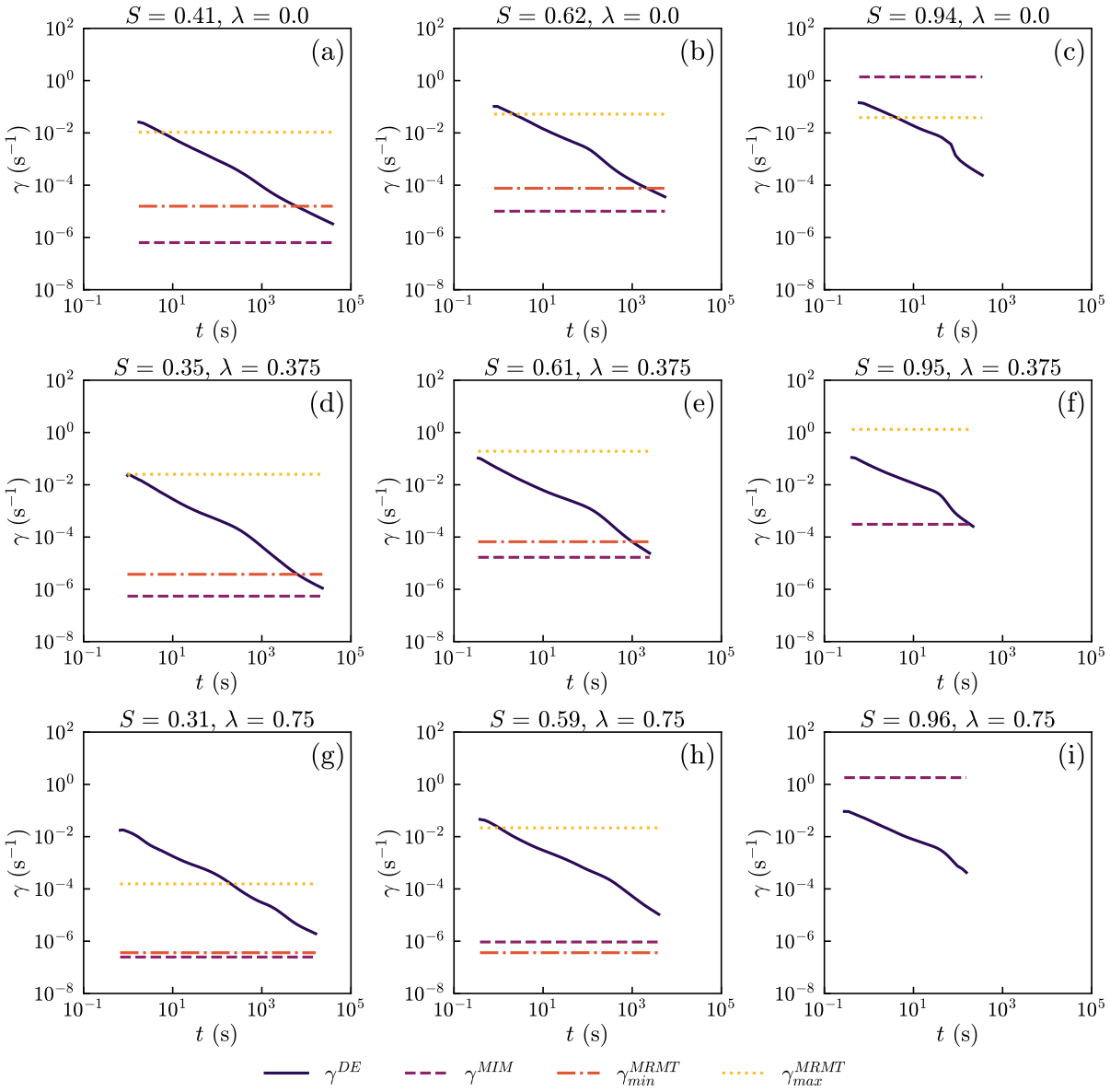

Figure S3: The mass transfer coefficients γ plotted as a function of time at $\Delta P = 10$ kPa and selected S values for the three different pore networks. Note that γ values estimated below 10^{-8} s^{-1} are not shown.

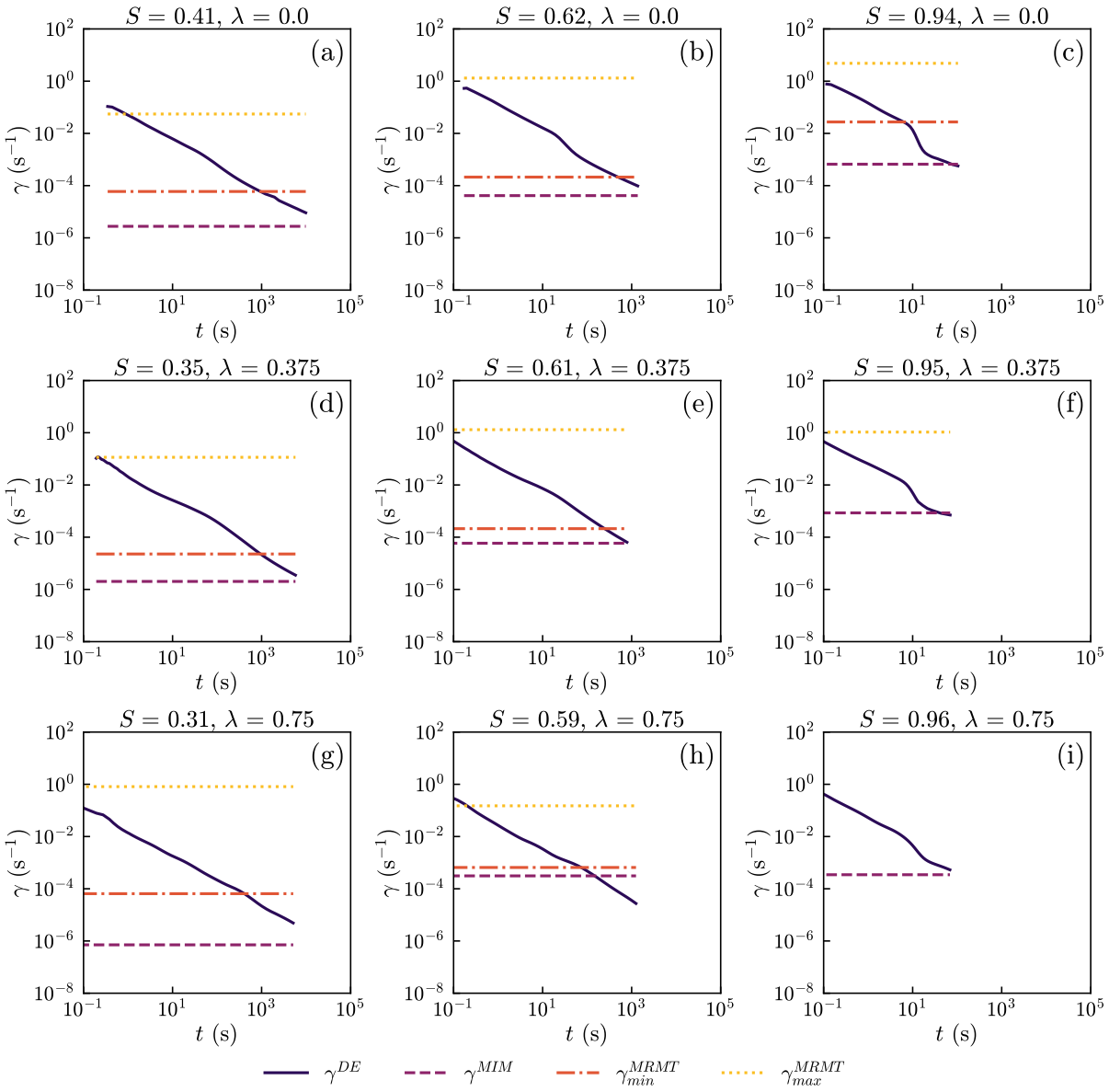

Figure S4: The mass transfer coefficients γ plotted as a function of time at $\Delta P = 50$ kPa and selected S values for the three different pore networks. Note that γ values estimated below 10^{-8} s^{-1} are not shown.

Figures S5 and S6 illustrate the temporal evolution of the effluent flux-averaged concentration $\langle C^f(t)\rangle$ versus time, along with the cutoff time t_2 estimated by the CTRW model, at $\Delta P = 10$ kPa and $\Delta P = 50$ kPa, respectively, for selected S values across the three pore networks.

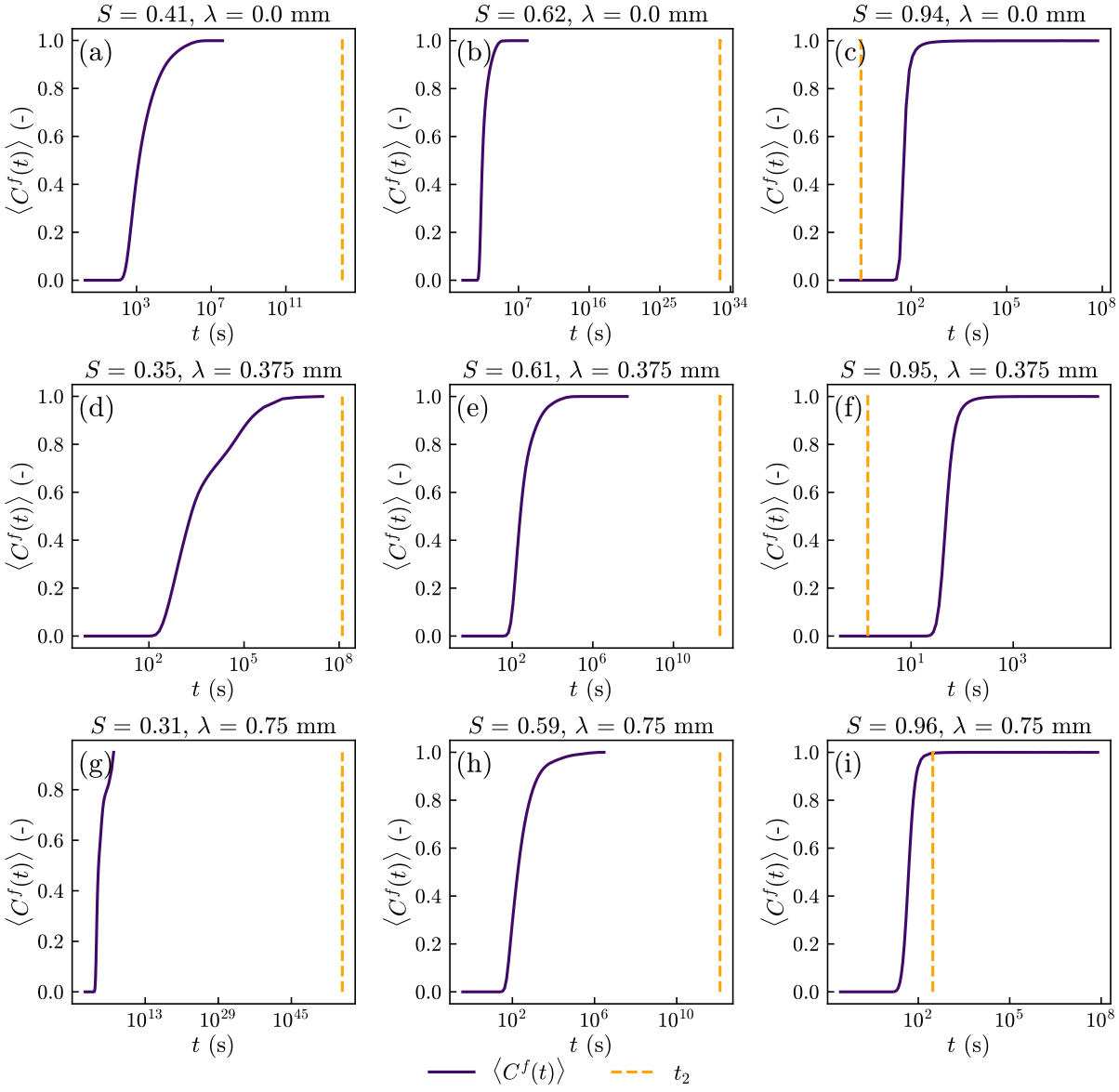

Figure S5: Effluent flux-averaged concentration BTC ($\langle C^f(t)\rangle$) illustrated as a solid line, plotted together with t_2, estimated by the CTRW model at $\Delta P = 10$ kPa and selected S values for the three different pore networks.

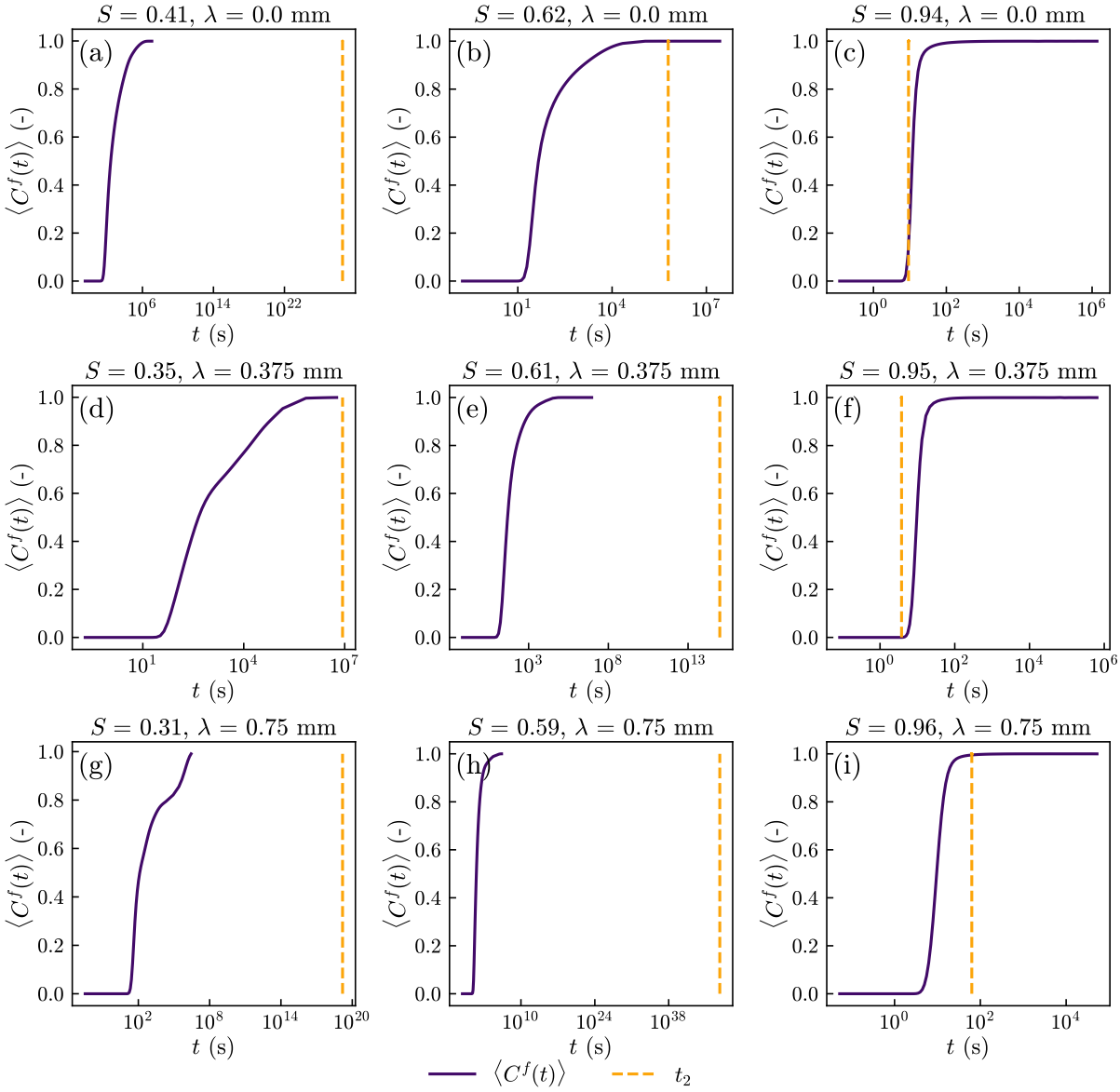

Figure S6: Effluent flux-averaged concentration BTC ($\langle C^f(t) \rangle$) illustrated as a solid line, plotted together with t_2, estimated by the CTRW model at $\Delta P = 50$ kPa and selected S values for the three different pore networks.

References

Van Offenwert, S., Cnudde, V., and Bultreys, T. (2019). Pore-scale visualization and quantification of transient solute transport using fast microcomputed tomography. *Water Resources Research*, 55(11):9279–9291.